(Proposal to Jefferson Lab PAC 40)

Measurement of Semi-Inclusive π° Production as Validation of Factorization

May 5, 2013

A. Camsonne, S. Covrig, P. Degtiarenko, R. Ent (spokesperson), D. Gaskell,
D. W. Higinbotham, M.K. Jones, C.E. Keppel, V. Kubarovksy, P. Nadel-Turoński,
B. Sawatzky, P. Solvignon, S.A. Wood, B. Wojtsekhowski
Jefferson Lab, Newport News, VA 23606

I. Albayrak, M. Carmignotto, J. Dénes-Couto, N. Hlavin, T. Horn (co-spokesperson),
F. Klein, M. Metz, B. Nepal
The Catholic University of America, Washington, DC 20064

C. Chen, M.E. Christy, Y. Han, N. Kalantarians, M. Kohl, L. Tang, J. Taylor
Hampton University, Hampton, VA 23668

A. Asaturyan, M. Khachatryan, A. Mkrtchyan, H. Mkrtchyan (co-spokesperson),
V. Tadevosyan (co-spokesperson), S. Zhamkochyan
A.I. Alikhanyan National Science Laboratory, Yerevan 0036, Armenia

C. Hyde, M. N. H. Rashad
Old Dominion University, Norfolk, Virginia

M. Guidal, C. Munoz Camacho, R. Paremuzyan
Institut de Physique Nucleaire d'Orsay, IN2P3, BP 1, 91406 Orsay, France

A. Ahmidouch, S. Danagoulian
North Carolina A&T University, Greensboro, NC 27411

G.M. Huber, W. Li
University of Regina, Regina, Saskatchewan, Canada, S4S 0A2

D. Dutta, J. Dunne
Mississippi State University, Mississippi State, MS

P. Markowitz
Florida International University, Miami, Florida

P. King, J. Roche
Ohio University, Athens, OH 45701

D. Day, D. Kellner, O. Rondon
University of Virginia, Charlottesville, VA, USA

D. Hamilton
University of Glasgow, Glasgow, Scotland, UK

S. Sirica
University of Ljubljana, Ljubljana, Slovenia

F. R. Wesselmann
Xavier University of Louisiana, New Orleans, LA

F. Benmokhtar

Duquesne University. Pittsburgh, PA

D. Androic
University of Zagreb. Bijenicka 32, HR-10000, Zagreb

and
The Neutral Particle Spectrometer collaboration
https://wiki.jlab.org/cuawiki/index.php/Collaboration

NEUTRAL PARTICLE SPECTROMETER (NPS) COLLABORATION

A. Camsonne, R. Ent, P. Nadel-Turoński, S.A. Wood, B. Wojtsekhowski
Jefferson Lab, Newport News, VA 23606

A. Asaturyan, A. Mkrtchyan, H. Mkrtchyan, V. Tadevosyan,
S. Zhamkochyan
A.I. Alikhanyan National Science Laboratory, Yerevan 0036, Armenia

M. Guidal, C. Munoz Camacho, R. Paremuzyan
Institut de Physique Nucleaire d'Orsay, IN2P3, BP 1, 91406 Orsay, France

I. Albayrak, M. Carmignotto, J. Dénes-Couto, N. Hlavin, T. Horn[1]
F. Klein, B. Nepal
The Catholic University of America, Washington, DC 20064

C. Hyde, M.N.H. Rashad
Old Dominion University, Norfolk, Virginia

P. King, J. Roche
Ohio University, Athens, OH 45701

D. Day, D. Keller, O. Rondon
University of Virginia, Charlottesville, VA, USA

D. Hamilton
University of Glasgow, Glasgow, Scotland, UK

S. Sirca
University of Ljubljana, Ljubljana, Slovenia

[1] Contact person: hornt@jlab.org

Executive Summary

The neutral pion electroproduction reaction is an important yet often neglected tool in our study of hadron structure by semi-inclusive deep inelastic scattering (SIDIS). The SU(3) wave function of π° does not allow apparent use for flavor decomposition in up and down quarks in the valence quark region, as enabled by charged-pion SIDIS processes. Yet, this same underlying wave function allows excellent use for systematic studies, to validate the prospective SIDIS science output at a 12-GeV JLab.

The exciting prospects of the SIDIS program are intertwined with our basic understanding of SIDIS at 11 GeV kinematics accessible in the high-luminosity Halls. These basic cross sections are needed to underpin our understanding of the anticipated factorization in hard electron-quark scattering (with dependence on Bjorken x) and the subsequent quark $\rightarrow$ pion fragmentation (with dependence on the fractional energy of the pions z), the so-called (x, z) factorization, and any subsequent dependence on low pion transverse momentum.

In SIDIS π° electroproduction, the lack of diffractive ρ contributions, the lack of pole contributions and thus radiative tail contributions at large z, the reduced nucleon resonance contribution (as for example compared to $ep \rightarrow e'\pi^-\Delta^{++}$), and the proportionality to an average fragmentation function, are all points in favor to validate low-energy (x, z) factorization required to substantiate the SIDIS science output.

A magnetic spectrometer setup and correlated precisions cross sections is very well suited to validate the SIDIS basic framework, as well supported by the 6-GeV JLab results [1]. Here, we plan to augment a series of measurements of the transverse momentum dependence of semi-inclusive charged-pion production (E12-09-017) with neutral-pion production measurements, acquired simultaneous with a companion proposal submitted to PAC40 to measure Deep Virtual Compton Scattering (DVCS) and Deep Virtual Neutral-Pion Production (DVNP). The proposed experiment covers the same phase space in x, Q^2, z and $P_{h\perp}$ as the approved E12-09-017 experiment, and uses the same basic setup as the DVCS and DVNP companion proposal (but only a subset of kinematics and beam time).

The measurement can be well performed using the existing and well-understood Hall C High-Momentum Spectrometer to detect the scattered electrons to precisely determine the electron scattering kinematics. The neutral pion will be detected by measurement of its $\gamma\gamma$ decay products in a dedicated new neutral-pion detector. We plan to use a high-resolution lead-tungstate $PbWO_4$ detector as 25 msr neutral-pion spectrometer (NPS). The NPS will be remotely rotated using cantelevered platforms of the SHMS spectrometer. A resistive sweeping magnet of 0.3 Tm reduces electromagnetic backgrounds. The NPS has a general setup that is common for this proposal, the DVCS/DVNP companion proposal, and a wide-angle compton scattering proposal. A more detailed description of this setup, including realistic background simulations that show the luminosity accessible with this setup as a function of angle, is given in a separate NPS document [2]. Given that the π° acceptance and kinematics determination are predominantly determined by geometry, we anticipate high-precision ($\sim 3\%$) basic (e,e$'\pi^\circ$) cross section measurements for a 10 cm long LH2 target and a modest beam current.

The proposed cross section measurements will provide basic tests of the theoretical understanding of SIDIS in terms of factorized parton distributions and fragmentation functions. Such neutral-pion precision cross section measurements will provide a critical foundation to validate the entire SIDIS program in studying the partonic structure of the nucleon, a now-flourishing physics program at Jefferson Lab spearheaded by members of this collaboration. The collaboration is keen to augment this knowledge in the 12-GeV era, and plans to seek funding for the construction of the NPS. The total beam time request corresponds to 25 PAC days, all in parallel with a companion DVCS/DVNP proposal submitted to PAC-40 as one single run group.

Contents

I. INTRODUCTION

Much is known about the light-cone momentum fraction, x, and virtuality scale, Q^2, dependence of the up and down quark parton distribution functions (PDFs) in the nucleon. In contrast, very little is presently known beyond these one-dimensional characterizations of nucleon structure, for instance about the dependence of these functions on their transverse momentum $\mathbf{p}_T$. One of the impacts of nucleon structure beyond the one-dimensional picture is the introduction of possible orbital motion of partons.

Increasingly precise studies of the nucleon spin sum rule [3–6] strongly suggest that the net spin carried by quarks and gluons does not account completely to the net value of the spin of the nucleon, and therefore an orbital angular momentum contribution of partons to the spin of the nucleon must be significant. This in turn implies that transverse momentum of quarks should be non-zero and correlated with the spin of the nucleon itself.

Once one realizes that transverse motion of partons is important, naturally arising questions include: what are the flavor and helicity dependence of the transverse motion of quarks and gluons; what is the appropriate formalism for a description of transverse motion of quarks from a theoretical point of view; but even more important: and how can these be measured experimentally?

It has been long realized that more stringent tests of the quark-parton model arise from more exclusive hadron production experiments. In particular, processes whose common feature is the tagging of the active parton provide unique tools for probing the flavor, transverse momentum, and spatial structure of the nucleon. The most general case of those is the semi-inclusive deep inelastic scattering (SIDIS) process in which one produces any number of final-state particles and tags the one that contains the active parton.

In SIDIS there exist extra kinematical degrees of freedom associated with the detected hadron. With the positive z-axis in the direction of the electromagnetic current, two further variables can be chosen to characterize the problem: the hadron transverse momentum $P_{h\perp}$ and the elasticity z. As a result, there will be in general four structure functions for the $(e, e'\pi)$ coincidence process, the usual longitudinal and transverse structure functions and two additional interference structure functions. Measurements of the $\cos(\phi)$ and $\cos(2\phi)$ dependencies to constrain these interference structure functions are now thought to shed light on the transverse motion of quarks, assuming parton dynamics. Within this proposal, we will mostly concentrate on a $P_{h\perp}$ region where we have access to the full ϕ acceptance, such that in principle we can remove sensitivity to these interference structure functions in SIDIS kinematics by integration.

As compared to deep-inelastic scattering, the inclusive hadron production process can lead to flavor decomposition of the contributions of transverse momentum widths. This correlation has recently been more rigorously worked out as part of the transverse momentum dependent (TMD) parton distribution formalism. There are indications of an x, energy, and flavor dependence of the widths of these functions. Further understanding of the underlying parton dynamics of the SIDIS process is particularly important at the modest energies of JLab where deviations of the Leading-Order factorized picture likely contribute. The $z \to 1$ limit is here of special interest from the perspective of hadron mass corrections, both in terms of finite values of target mass M^2/Q^2 and produced hadron mass m_π^2/Q^2 relative to the virtual photon mass Q^2 (~ 4 GeV^2) [7].

Having cross section data in hand for the proposed neutral-pion SIDIS experiment, combined with the anticipated precision data for SIDIS with charged-meson production of E12-09-017, one may also make comparisons between π^+, π^- and π°, which would allow for a precision verification of the often-assumed relation $\pi^\circ = (\pi^+ + \pi^-)/2$. One would anticipate that in the limit $z \to 1$ the behavior may differ from this often-used yet naive assumption given complications in the SIDIS framework at moderate energies, in the SIDIS data analysis and assumed factorization, and assumptions on the fragmentation process. In the kaon case, for example, there seems a huge difference between $D_u^{K^+}$ and $D_{\bar{s}}^{K^+}$, which naively would be the same given that $K^+ = u\bar{s}$. Of course the masses of u and s are much different, which may lead one to believe that $D_{\bar{s}} > D_u$, but the opposite seems true. In the limit $z \to 1$ one would anticipate the behavior of π° to differ from that for $(\pi^+ + \pi^-)/2$, given that the exclusive limit has no pole contributions. Thus, comparisons of π° and $\pi^\pm$ will provide valuable information on the size of non-leading twist contributions at JLab energies and potential further parton dynamics and

model extractions. As a by-product they would directly allow to revisit the inclusive-exclusive connection dating back to the 1970s in a new fashion, extending the realizations within the constituent quark model of duality in several symmetry breaking scenarios from charged-pion to neutral-pion electroproduction [8]. As indicated above, semi-inclusive data in the limit of $z \to 1$ would constrain target and hadron mass corrections [7]. Lastly, the neutral-pion data would be free from various complications of the charged-pion SIDIS analysis, allowing a solid experimental validation of assumed (x, z) factorization on which any partonic interpretation of SIDIS data hinges. Thus, the proposed measurements are both of fundamental and of practical value for the SIDIS studies at JLab and beyond as they will constrain our parton interpretation of SIDIS data.

A. Factorization in semi-inclusive deep inelastic scattering.

In semi-inclusive deep inelastic scattering, a hadron h (in our case a pion) is detected in coincidence with a scattered electron, with a sufficient amount of energy and momentum transferred in the scattering process. Under the latter conditions, the reaction can be seen as knockout of a quark and subsequent (independent) hadronization.

At high values of Q^2 and ν, the cross section (at leading order in the strong coupling constant α_s) for the reaction $N(e, e'\pi)X$ can be written in the following way (see Ref. [9]),

$$\begin{aligned} \frac{\frac{d\sigma}{d\Omega_e dE_e dz dP_{h\perp}^2 d\phi}}{\frac{d\sigma}{d\Omega_e dE_e}} &= \frac{dN}{dz} b e^{-bP_{h\perp}^2} \frac{1+Acos(\phi)+Bcos(2\phi)}{2\pi}, \\ \frac{dN}{dz} &\sim \sum_i e_i^2 \; q_i(x, Q^2) \; D_{q_i \to \pi}(z, Q^2), \end{aligned} \tag{1}$$

where i denotes the quark flavor and e_i is the quark charge, and the fragmentation function $D_{q_i \to \pi}(z, Q^2)$ gives the probability for a quark to evolve into a pion π with a fraction z of the quark (or virtual photon) energy, $z = E_\pi/\nu$. The first part of this formula expresses that the cross section factorizes into the product of the virtual photon–quark interaction and the subsequent quark hadronization. A consequence of factorization is that the fragmentation function is independent of x, and the parton distribution function $q_i(x, Q^2)$ independent of z. Both parton distribution and fragmentation functions, however, depend on Q^2 through logarithmic Q^2 evolution [10]. The second part describes the dependence on the transverse momentum $P_{h\perp}$, assumed to be Gaussian, and the general dependence [11] of the cross section in the unpolarized case on the angle ϕ, the angle between the electron scattering plane and the pion production plane, with A and B, reflecting the interference terms σ_{LT} and σ_{TT}, respectively, being functions of $x, Q^2, z, P_{h\perp}$.

If one neglects the dependence of the cross section on the pion transverse momentum $P_{h\perp}$ and the angle ϕ, the SIDIS cross section as given in Eq. (1) can be written as

$$\sigma \propto \sum_i q_i(x, Q^2) \; D_{q_i \to \pi}(z, Q^2). \tag{2}$$

(At higher orders one has to worry about gluon fragmentation functions, but this can be neglected for the energy and momentum transfers under consideration here [12]). The question is how well this factorization into independent functions of x and z is fulfilled in practice.

Initial investigations of the hadronization process were made in electron–positron annihilation and in deep inelastic scattering. By now a wealth of data has been accumulated to parametrize the fragmentation functions as function of z and Q^2. It is well known that for the case of SIDIS one needs to be able to separate pions directly produced by the struck quark (termed "current fragmentation") from those originating from the spectator quark system ("target fragmentation"). This has been historically done for high-energy SIDIS by using separation in rapidity, η. Early data from CERN [13, 14] suggested that a difference in rapidities, $\Delta\eta$, between pions produced in the current and target fragmentation regions ("rapidity gap") of at least $\Delta\eta \approx 2$ is needed to kinematically separate the two regions. Later, it was realized that such kinematic separation is even possible at lower energies, or low W^2, if one considers only electroproduced pions with large elasticity z, *i.e.*, with energies close to the

maximum energy transfer [14, 15]. This is what experiments at a 6-GeV or 12-GeV Jefferson Lab hinge on. In the end, factorization in terms of a hard scattering and subsequent hadronization needs to be proven experimentally, to provide a solid foundation for any partonic interpretation of SIDIS data.

At Jefferson Lab this started in Hall C, where E00-108 [16] measured the ^{1,2}H(e,e$'\pi^{\pm}$)X unseparated cross sections, predominantly at $x = 0.32$. The data conclusively showed the onset of the quark-hadron duality phenomenon in the semi-inclusive (e,e$'\pi$) process, and the relation of this to the high-energy factorization ansatz of subsequent electron-quark scattering and quark $\rightarrow$ pion production. Agreement between data and Monte Carlo simulation, based upon CTEQ5M parton distributions [17] and BKK fragmentation functions [12], was found to be excellent for $z < 0.65$ (or $M_x^2 > 2.5$ GeV^2: note that within the E00-108 kinematics $P_{h\perp} \sim 0$, and M_x^2 is almost directly related to z, as $W'^2 \equiv M_x^2 = M_p^2 + Q^2(1/x - 1)(1 - z)$. Simple ratios constructed from the data following quark-parton model descriptions were found to be remarkably close to the near-independence of z as anticipated in the high-energy limit (at leading order in α_S).

These findings have led to a rich and industrious SIDIS program at JLab at both 6 GeV, and soon 12 GeV. Nonetheless, one should keep in mind that the partonic interpretation is only as good as the experimental validation of (x, z) factorization, which we will argue is the reason to require precise neutral-pion cross section data to accompany anticipated charged-pion cross section data.

II. PHYSICS FORMALISM

The so-called Transverse Momentum Dependent factorization was first shown [18] for Semi-Inclusive Deep Inelastic scattering (SIDIS), $lN \rightarrow l'hX$ for high values of $Q^2 \gg \Lambda_{QCD}^2$ and moderate values of transverse momenta of the produced hadron, $P_{h\perp} \sim \Lambda_{QCD}$. High Q^2 assures QCD factorization, while the small transverse momenta $P_{h\perp}$ of the electro-produced hadrons make it sensitive to intrinsic motion of the partons. The factorization is formulated in terms of so-called Transverse Momentum Dependent (TMD) parton distribution (and fragmentation functions), that in addition to their usual dependence on x and Q^2 also depend on the transverse momentum of partons $\mathbf{p}_T$.

The unpolarized SIDIS cross section [19, 20] can be written in terms of four structure functions

$$\frac{d\sigma}{dx\,dy\,d\psi\,dz\,d\phi_h\,dP_{h\perp}^2} = \frac{\alpha^2}{xyQ^2}\,\frac{y^2}{2\,(1-\varepsilon)}\left(1+\frac{\gamma^2}{2x}\right)\Big\{F_{UU,T} + \varepsilon\,F_{UU,L} + \sqrt{2\,\varepsilon(1+\varepsilon)}\,\cos\phi_h\,F_{UU}^{\cos\phi_h} + \varepsilon\cos(2\phi_h)\,F_{UU}^{2\cos\phi_h}\Big\} \tag{3}$$

where the experimentally measured structure functions are $F_{UU,T} + \varepsilon F_{UU,L}$ (separable through Rosenbluth separations as *e.g.* in experiment E12-06-104), which are ϕ_h independent, and $F_{UU}^{\cos\phi_h}$ and $F_{UU}^{2\cos\phi_h}$ which are $\cos\phi_h$ and $\cos 2\phi_h$ modulations, respectively.

At leading twist, the spin structure of a spin-1/2 hadron can be described by 8 TMDs [19–21]. Each TMD represents a particular physical aspect of spin-orbit correlations at the parton level. The dependence of the SIDIS cross section on the azimuthal angle of the electro-produced hadron with respect to the lepton scattering plane and on the nucleon polarization azimuthal angle allows a term-by-term separation of the different azimuthal contributions to the measured unpolarized and polarized cross sections and spin asymmetries. The unpolarized SIDIS cross-section can be used not only to study the unpolarized TMD distribution function $f_{q/p}(x, \mathbf{p}_T^2)$ and the unpolarized TMD fragmentation function $D_{h/q}(z, \mathbf{k}_T^2)$ that encode the intrinsic dynamics of unpolarized partons, but also the Boer-Mulders distribution and the Collins fragmentation functions, which carry information about the dynamics of transversely polarized partons inside the hadron and give rise, for instance, to a $\cos 2\phi_h$ modulation of the cross section.

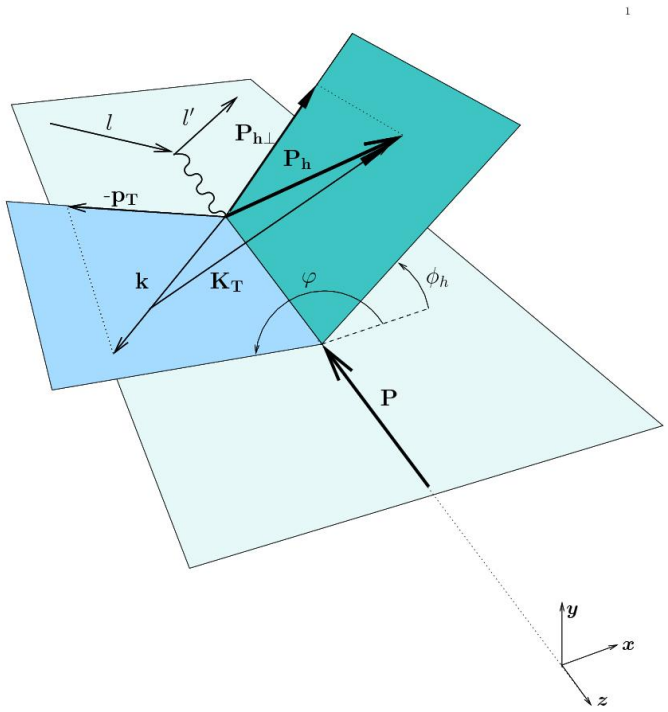

FIG. 1: Kinematics of the SIDIS process in the $\gamma^* p$ center of mass frame.

The existence of partonic intrinsic transverse momenta is unequivocally signaled by a $\cos\phi_h$ modulation, which is a subleading twist effect suppressed by one power of Q. This contribution to the unpolarized cross section consists of a purely kinematical term, the Cahn effect [22], proportional to the convolution of unpolarized distribution and fragmentation functions, together with other twist-3 contributions, as pointed out in Ref. [20].

We define here the following variables describing the kinematics:

$$\begin{aligned} s &= (p+l)^2 \quad \text{energy of the ep system} \\ W^2 &= (p+q)^2 \quad \text{energy of the } \gamma^*\text{p system} \\ Q^2 &= -q^2 > 0 \qquad \text{photon's virtuality} \end{aligned} \tag{4}$$

and

$$x = \frac{Q^2}{2\,P\cdot q}, \;\; y = \frac{P\cdot q}{P\cdot l}, \;\; z = \frac{P\cdot P_h}{P\cdot q}, \;\; \gamma = \frac{2Mx}{Q}, \;\; \varepsilon = \frac{1-y-\frac{1}{4}\gamma^2 y^2}{1-y+\frac{1}{2}y^2+\frac{1}{4}\gamma^2 y^2}. \tag{5}$$

A partonic interpretation of the measured structure functions can be obtained as convolution of distribution and fragmentation functions [19, 20]

$$F_{AB} = \mathcal{C}[w\,f\,D], \tag{6}$$

where $\mathcal{C}[...]$ is defined as

$$\mathcal{C}\big[w\,f\,D\big] = x\sum_a e_a^2 \int d^2\boldsymbol{p}_T\, d^2\boldsymbol{k}_T\, \delta^{(2)}\big(z\boldsymbol{p}_T + \boldsymbol{k}_T - \boldsymbol{P}_{h\perp}\big)\, w\left(\boldsymbol{p}_T, -\frac{\boldsymbol{k}_T}{z}\right) f^a(x,p_T^2)\, D^a(z,k_T^2), \tag{7}$$

and $w\left(\boldsymbol{p}_T, -\frac{\boldsymbol{k}_T}{z}\right)$ is a function depending on partonic momenta, $f^a(x,p_T^2)$ is a TMD parton distribution and $D^a(z,k_T^2)$ is a transverse-momentum dependent fragmentation function.

Eq. 7 indicates a summation over the various quark flavors. Thus, to go beyond and study a possible flavor dependence of the TMDs one has to measure different species of hadrons produced. This can be most readily accomplished with charged-pions and charged-kaons (and neutral pions). Within a simple gaussian Ansatz for TMDs one can show [23] that $\mathbf{P}_{h\perp} = z\mathbf{p}_T + \mathbf{k}_T$ and thus $\langle \mathbf{P}_{h\perp}^2 \rangle = z^2 \langle \mathbf{p}_T^2 \rangle + \langle \mathbf{k}_T^2 \rangle$.

The fragmentation process is traditionally described with both "favored" and "unfavored" fragmentation functions $D^+(z, \mathbf{k}_T)$ and $D^-(z, \mathbf{k}_T)$, that refer to cases when the electro-produced pion either contains or does not contain the same flavor as the struck quark. In the latter unfavored case, the quark content is picked up from the vacuum, and the process of fragmentation is suppressed.

At small values of $\mathbf{p}_T$ one expects that distribution of momenta are approximately gaussian [23] and experimental data confirm this finding. Hard QCD processes are expected to generate large non-Gaussian tails for $P_{h\perp} \gg \Lambda^2_{QCD}$. However, at small $P_{h\perp} < 0.5$ GeV, the subject of this proposal, one might use TMD factorization without worrying about gluon radiation effects. The TMDs can then be parametrized as gaussians

$$\begin{aligned} f_1^q(x, p_T^2) &= f_1^q(x) \frac{1}{\pi \langle p_T^2 \rangle} \exp\left(-\frac{\mathbf{p}_T^2}{\langle p_T^2 \rangle}\right), \\ D_{1q}^h(z, K_T^2) &= D_{1q}^h(z) \frac{1}{\pi \langle k_T^2 \rangle} \exp\left(-\frac{\mathbf{k}_T^2}{\langle k_T^2 \rangle}\right) \end{aligned} \tag{8}$$

where the widths of distributions are $\langle p_T^2 \rangle$ and $\langle k_T^2 \rangle$. Usually these widths are taken to be flavor independent, but this is just an assumption.

The two interference structure functions of Eqn. (6) introduce $\cos\phi_h$ and $\cos 2\phi_h$ modulations (with polarized beam one would introduce a fifth structure function with an associated $\sin\phi_h$ modulation that is a final-state interaction or higher-twist effect). These modulations correspond to the factors A and B in the earlier schematic Eqn. (1). TMD factorization allows for an expansion of the structure functions in powers of $1/Q$ and express them in terms of convolutions of transverse-momentum dependent distribution and fragmentation functions, alluded to above. In our case, with unpolarized structure functions, the Cahn effect and the Boer-Mulders effect come into play, with the Cahn effect (Cahn) a purely kinematical effect proportional to the quark transverse momentum, and the Boer-Mulders effect (BM) describing the correlation between the transverse polarization and transverse momentum of quarks in an unpolarized nucleon.

The longitudinal-transverse structure function $\sqrt{2\,\varepsilon(1+\varepsilon)}\cos\phi_h\, F_{UU}^{\cos\phi_h}$ is related to the $\cos\phi_h$ amplitude and suppressed as $1/Q$. Subsequent contributions are suppressed like $1/Q^3$. In the Wandzure-Wilczek approximation, the structure function has two contributions, schematically: $F_{UU}^{\cos\phi_h} \sim (1/Q)$ Cahn + $(1/Q)$ BM. Similarly, in a simplified form the transverse-transverse structure function $\varepsilon\cos(2\phi_h)\, F_{UU}^{2\cos\phi_h}$ has the following schematic dependence: $F_{UU}^{2\cos\phi_h} \sim$ BM $+(1/Q^2)$ Cahn. Recent results from both HERMES [24] and COMPASS [25] experiments find a strong z dependence of measured azimuthal asymmetries, notably at large $z > 0.5$, and a variation of positively-charged and negatively-charged pions, most noticable at large z and larger $P_{h\perp} > 0.5$ GeV, but present at smaller $P_{h\perp}$.

The possibility of a study of the k_t widths of up and down quarks under the main assumption that the fragmentation functions do not depend on quark flavor (and multiple other assumptions) was first indicated following the results of the E00-108 experiment in Hall C at Jefferson Lab [26]. Ongoing work also shows indications of an x [27] and energy [28] dependence of these k_t widths.

A recent study [28] analyzed these data in combination with the CLAS data [29], and concluded that in the kinematics similar to the CLAS data, the Hall C data could be relatively well described by a Gaussian model with average transverse momentum width of 0.24 GeV^2. The good description of the $\pi^\pm$ cross sections from different targets was argued to indicate that the assumption of flavor-independent Gaussian widths for both the transverse widths of quark and fragmentation functions was reasonable, in the valence-x region for $z = 0.55$.

This can only be considered as suggestive at best, due to the limited kinematic range covered and the assumptions. Many of these limitations could be removed with the envisioned 12-GeV program covering a wide range of Q^2 (to resolve additional higher twist contributions), full coverage in ϕ, a larger range of $P_{h\perp}$, and a wide range in z (to distinguish quark width terms, weighted by powers of z, from fragmentation widths, which likely vary slowly with z). For instance, these goals should be attainable with the approved E12-09-017

experiment, emphasizing semi-inclusive charged-pion electroproduction. However, for instance the assumption that only two fragmentation functions are needed for charged pions originating from valence quarks requires additional consistency checks by including the π° final state. This combined with that analysis of semi-inclusive meson electroproduction data at moderate energies can come with theoretical (higher-twist, target-mass) and experimental pitfalls, leads to the requirement of a companion 12-GeV program including precision π° cross section scans as functiion of x and z. Such a consistency verification is required to validate the SIDIS framework and the resulting nucleon structure information.

III. PITFALLS IN SIDIS ANALYSIS

Here we will describe complications in the SIDIS data analysis that warrant a precision determination of (x, z) factorization with neutral-pion data. We will first shortly revisit the empirical evidence for (x, z) factorization at 6-GeV JLab energies, and then go into some examples of the complications in the SIDIS data analysis, and why the SIDIS (e,e$'\pi^\circ$) data can further elucidate these complications and allow a quantification of the partonic interpretation of SIDIS data at a 12-GeV JLab. We will then use the extraction of the d/u ration as key example, as this has been difficult to get right in SIDIS analysis, even if the data seem to indicate to follow the SIDIS formalism.

A. Evidence for (x, z) Factorization at a 6-GeV JLab

The E00-108 experiment in Hall C was the first SIDIS experiment approved at JLab. E00-108 measured the ^{1,2}H(e,e$'\pi^\pm$)X cross sections at $x = 0.32$, and compared the measured cross sections with the results of a SIDIS simulation in Fig. 2, as a function of z [16]. The SIDIS simulation followed the high-energy factorization ansatz of subsequent electron-quark scattering, as parametrized by CTEQ5M parton distributions [17], and quark $\rightarrow$ pion production, as described in the simulation by the BKK fragmentation functions [12].

Agreement between data and Monte Carlo simulation was found to be excellent for $z < 0.65$ (or $M_x^2 > 2.5$ GeV^2: note that within the E00-108 kinematics $P_{h\perp} \sim 0$, and M_x^2 is almost directly related to z, as $W'^2 \equiv M_x^2 = M_p^2 + Q^2(1/x - 1)(1 - z)$. Hence, the large "rise" in the data with respect to the simulation at $z > 0.8$ mainly reflects the $N - \Delta(1232)$ region. Indeed, if one considers a ^{1}H(e,e$'\pi^-$)X spectrum as function of missing mass of the residual system X, one sees only one prominent resonance region, the $N - \Delta$ region. Apparently, above $M_x^2 = 2.5$ GeV^2 or so, there are already sufficient resonances to render a spectrum mimicking the smooth z-dependence as expected from the Monte Carlo simulation following the factorization ansatz. Simple ratios constructed from the data following quark-parton model descriptions were found to be remarkably close to the near-independence of z as anticipated in the high-energy limit (at leading order in α_S). Further examples of empirical evidence of the onset of a partonic interpretation of SIDIS cross sections and ratios at JLab energies, and the inherent empirical evidence for (x, z) factorization, are presented in a large archival paper [1]. These results are the foundation that led to the followup 6-GeV SIDIS program and the large number of SIDIS experiments foreseen at a 12-GeV JLab.

B. Diffractive ρ

Some of the detected events may originate from the decay of diffractive vector meson production. The underlying physics of this process, which can be described as that the virtual photon fluctuates into a vector meson, which subsequently can interact with the nucleon through multiple gluon (Pomeron) exchange, is distinctively different from the interaction of a virtual photon with a single current quark. We used SIMC - the Halls C and A Monte Carlo simulation package including radiative effects - to evaluate such a diffractive ρ meson contribution.

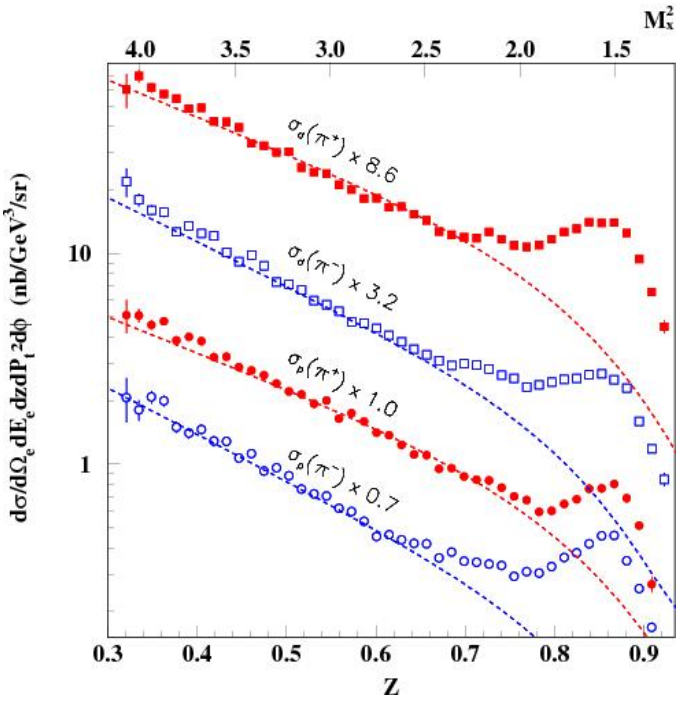

FIG. 2: The $^{1,2}H(e,e'\pi^{\pm})X$ cross sections at x=0.32 as a function of z in comparison with Monte Carlo simulations (dashed curves) starting from a fragmentation ansatz. The various cross sections have been multiplied as indicated for the purpose of plotting.

The p(e,e′ρ°)p cross section calculation was based on the PYTHIA [30] generator, adopting similar modifications as implemented by the HERMES collaboration to describe lower-energy processes [31]. Additional modifications were implemented to improve agreement with ρ^0 cross section data from CLAS in Hall B at Jefferson Lab [32].

The p(e,e′ρ°)p cross section can be written as

$$\sigma^{ep\to\rho p}(\nu,Q^2) = \Gamma_T\,(1+\epsilon R)\left(\frac{M_\rho^2}{M_\rho^2+Q^2}\right)^n \sigma^{\gamma p\to\rho p}, \tag{9}$$

where Γ_T is the transverse photon flux factor, $R=\sigma_L/\sigma_T$ is the ratio of longitudinal to transverse cross sections, $\left(\frac{M_\rho^2}{M_\rho^2+Q^2}\right)^n$ ($n=2$ in PYTHIA) is an additional factor that accounts for the suppression of the cross section from virtual photons, and $\sigma^{\gamma p\to\rho p}$ is the photoproduction cross section. The modifications to the PYTHIA model implemented for this analysis mimic those implemented by the HERMES collaboration:

1. The calculation of Γ_T was performed with no high-energy approximations
2. An improved parametrization of $R=\sigma_L/\sigma_T$
3. Replacement of the exponent $n=2$ with $n\approx 2.6$, more consistent with lower energy data

The t dependence of the ρ° cross section is parametrized as

$$\frac{d\sigma}{d|t'|} = \sigma^{ep\to\rho p}(\nu,Q^2)be^{-b|t'|}, \tag{10}$$

where $t'=t-t_{min}$ (<0 for electroproduction) and b is the slope parameter. Note that at $t'=0$, b also impacts the overall scale of the forward cross section. The HERMES/PYTHIA model assumed a value of $b\approx 7$ GeV^{-2} for all energies. However, CLAS data suggested that this constant value of b did not adequately describe the t' dependence at JLab energies. The model used in SIMC fits b as a function of $c\Delta\tau$ (the vector meson formation

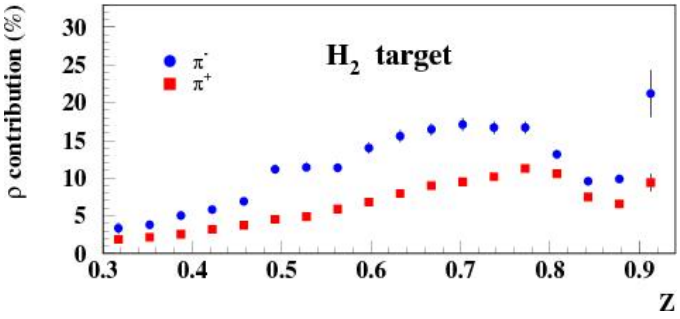

FIG. 3: Relative contribution of the events from $p(e,e'\rho^\circ)p$ reaction in Semi-Inclusive $\pi^\pm$ production experimental data for z-scan on hydrogen target.

time). Above $c\Delta\tau = 2$ fm, b was taken to be a constant value of 7.0 GeV^{-2}, while for $c\Delta\tau < 2$ fm, b increased from 1.0 GeV^{-2} to 7.0 GeV^{-2} between $c\Delta\tau = 0.4$ fm and 2 fm.

Using the above model, the fraction of events due to pions from the decay of produced ρ mesons was estimated to range from a few percent at low z to about 15% at $z = 0.6$ (see Fig. 3), and was subtracted on bin by bin basis.

The SIMC determination of the exclusive ρ° contribution to the semi-inclusive yield was also checked independently using a program and model developed by the CLAS collaboration [33]. The two calculations were found to agree to about the 10% level. There was uncertainty related to the choice of the parametrization for the ρ^o cross sections in the SIDIS data analysis. A slight variation (by ∼10%) of the model parameters resulted in the systematic uncertainty of up to $\approx 2.5\%$.

The advantage of SIDIS π° electroproduction is the lack of diffractive ρ contributions.

C. Radiative Tails

The radiative tail from exclusive events is the dominant correction for data at large z, $z > 0.8$ or so. For example, in the E00-108 data analysis for $z \gtrsim 0.9$ the contributions from exclusive pions become more than 50%.

Essentially all of the events that "radiate in" to a given bin come from either: (i) incoming electrons with a lower actual energy than the nominal beam energy, because they have radiated a photon; or (ii) scattered electrons with higher energy than the one measured in the spectrometer, because they radiated a photon. In both cases, the value of ν at the vertex is lower than the reconstructed one, hence z is larger and W' is smaller than the nominal value.

The radiative tails within our semi-inclusive pion electroproduction data were estimated using the Monte Carlo package SIMC. The radiative correction formula coded is based on the work of Mo and Tsai [34], which originally was derived for inclusive electron scattering, but was modified for use in coincidence experiments [35]. The original formulation of the radiative correction procedure used in SIMC was for the $(e,e'p)$ reaction. Details of the implementation, and the extension to kaon electroproduction are described in Ref. [36]. The formula were further extended to pion electroproduction in Ref.l [37].

As a cross-check, we also estimated radiative corrections using the code POLRAD. The standard FORTRAN code POLRAD-2.0 [38] was written for radiative correction (RC) calculations in inclusive and semi-inclusive deep-inelastic scattering of polarized leptons by polarized nucleons and nuclei. The program, which is based theoretically on the original approach proposed in the Ref. [39], was created to suit the demands of experiments with fixed polarized nuclear targets and at a collider. A new version of POLRAD [40] was created to calculate the RC for semi-inclusive (polarized) experiments. In this case the cross section depends additionally on the variable z.

The radiative corrections calculated with POLRAD-2.0 are in good agreement with SIMC. On average the RC's are on the level of $\sim 6-8\%$ for all data sets at $z < 0.7$ and reach $\sim 15\%$ at $z \gtrsim 0.9$. The relative values

TABLE I: The values of radiative corrections for z-scan data.

x	z	Q^2 (GeV/c)^2	π^+_H (%)	π^-_H (%)	π^+_D (%)	π^-_D (%)
0.32	0.37	2.31	1.6±0.2	3.3±0.3	2.1±0.2	3.2±0.3
0.32	0.42	2.31	2.4±0.2	4.1±0.4	2.8±0.3	3.9±0.4
0.32	0.49	2.31	3.4±0.3	5.1±0.5	3.8±0.4	4.8±0.5
0.32	0.55	2.31	4.5±0.5	6.2±0.6	4.9±0.5	5.8±0.6
0.32	0.64	2.31	5.9±0.6	7.5±0.8	6.2±0.6	7.0±0.7
0.32	0.74	2.31	7.8±0.8	9.3±0.9	8.1±0.8	8.8±0.9
0.32	0.85	2.31	10.8±1.1	11.9±1.2	11.0±1.1	11.5±1.2
0.32	0.97	2.31	18.3±1.3	18.5±1.9	18.3±1.8	18.3±1.8

of radiative corrections at E00-108 kinematic settings are listed in Table I.

Exclusive Pions: Subtraction of radiative events coming from the exclusive reactions $e+p \rightarrow e'+\pi^+ +n$ and $e+n \rightarrow e'+\pi^- +p$ requires a model for the cross section of exclusive pion electroproduction that is valid for a large range of W (from the resonance region to $W \approx 2.5$ GeV) at relatively large Q^2. The model used in this analysis started with the parametrization of exclusive π^+ and π^- production cross section data from [41] at $W \approx 2.2$ GeV and $Q^2 = 0.7$ and 1.35 (GeV/c)^2. This parametrization describes the more recent data taken at Jefferson Lab as part of the Charged Pion Form Factor program [42–44] ($W = 1.95$ GeV, Q^2=0.6−1.6 (GeV/c)^2 and $W = 2.2$ GeV, Q^2=1.6, 2.45 (GeV/c)^2) reasonably well.

While the starting parametrization is appropriate for describing exclusive pion production above the resonance region, it does rather poorly for values of W significantly smaller than 2 GeV. Since no existing model or parametrization describes exclusive pion production both in the resonance region and at large W, we chose to adjust our starting model by-hand to give good agreement with the MAID model [45] of pion electroproduction in the resonance region. This by-hand adjustment began with the assumption that the longitudinal contribution was well described by the starting model, even at relatively low W. Discrepancies between the starting fit and the MAID calculation were attributed to the transverse cross section and were removed by assuming a more modest W dependence therein. We further simplified the model by assuming that the TT and LT interference terms mostly averaged to zero over our experimental acceptance so that they contributed negligibly to the radiative events.

We used the SIMC package with this modified model for exclusive π^+ electroproduction on the proton and for π^+ and π^- production on the deuteron for all the kinematic settings of E00-108. The contributions from exclusive pions were subtracted on a bin by bin basis. On average, the contribution from the exclusive tail was estimated to range from 5 to 15% as a function of z (at $z < 0.8$) (see Table II).

The radiative tail from exclusive events is clearly the dominant correction for the E00-108 data at $z > 0.8$. This will in general be the case for SIDIS data from JLab at 6-GeV or 12-GeV beam energies, albeit with variations with z and Q^2. For $z \gtrsim 0.9$ the contributions from exclusive pions can become more than 50%. Note that we also performed an alternative analysis using the code HAPRAD [46]. The two results agree to within $\pm 10-15\%$ in the relative contribution of the radiative tail due to the exclusive channels. Given the agreement and the relative contribution, the resulting uncertainty is estimated to be at the 1% level or less (for $z < 0.8$).

The advantage of SIDIS π° electroproduction is the lack of pole contributions, and thus radiative tail contributions at large z.

D. Nucleon Resonance Contributions

As noted earlier, for E00-108 kinematics, $P_{h\perp} \sim 0$, M_x^2 is almost directly related to z Hence, as illustrated in Fig. 2, the large "rise" in the data with respect to the partonic expectations, based upon a factorization ansatz of electron-quark scattering and subsequent quark-pion fragmentation, is mainly due to the introduction of the nucleon resonance region, or more specifically the $N-\Delta(1232)$ region, at $z > 0.7$. It is important to remember

TABLE II: The relative contribution of radiative exclusive tail for z-scan data.

x	z	Q^2 (GeV/c)^2	π^+_H (%)	π^-_H (%)	π^+_D (%)	π^-_D (%)
0.32	0.33	2.31	3.6±0.2	-	2.6±0.1	3.6±0.2
0.32	0.38	2.31	3.9±0.1	-	3.1±0.1	4.6±0.1
0.32	0.44	2.31	4.3±0.1	-	3.4±0.1	4.7±0.1
0.32	0.50	2.31	4.1±0.1	-	2.8±0.1	5.0±0.1
0.32	0.55	2.31	5.9±0.1	-	4.4±0.1	7.6±0.1
0.32	0.61	2.31	7.5±0.1	-	5.8±0.1	8.7±0.2
0.32	0.66	2.31	8.8±0.1	-	6.4±0.1	10.3±0.2
0.32	0.72	2.31	11.0±0.2	-	7.7±0.1	12.2±0.2
0.32	0.78	2.31	13.8±0.2	-	8.7±0.2	15.1±0.3
0.32	0.83	2.31	15.7±0.3	-	9.5±0.2	18.0±0.4
0.32	0.89	2.31	21.8±0.4	-	15.0±0.3	30.3±0.6
0.32	0.94	2.31	$\gtrsim$90	-	$\gtrsim$90	$\gtrsim$90

that the counter of this argument is that above $M_x^2 = 2.5$ GeV^2 or so (corresponding to $z < 0.7$ within the E00-108 kinematics), there are already sufficient resonances to render a spectrum with smooth z-dependence.

At 12-GeV energies, the accessible Q^2 for fixed x slightly grows, so the z value corresponding to $M_x^2 = 2.5$ GeV^2 changes. For a doubling of Q^2, the z value for instance would grow to $z = 0.85$ (for $x = 0.32$). Similarly, the z value where a partonic interpretation of SIDIS data at JLab energies will be relevant, will depend on the meson species measured. Separation of current and target region fragmentation, assumed to be required for (x, z) factorization, will be different for pions and kaons. This will impact the lower z value where a partonic interpretation of data within a SIDIS framework is relevant for JLab energies. Similarly, at the higher z values there are differences expected due to the specific ^{1}H(e,e$'m$)X nucleon resonance spectrum. In fact, the missing mass spectrum of residual state X will be different for various mesons m. It is well known that nucleon resonance excitations are most visible for the lower-lying (ground and) first-excited states, and less visible for heavier mass mesons m. It will also be different for neutral-pions versus charged-pions, due to specific strength on nucleon resonance excitations. For example, the $ep \to e'\pi^\circ\Delta^+$ is much reduced as compared to $ep \to e'\pi^-\Delta^{++}$, giving reason to expect the SIDIS (e,e$'\pi^\circ$) cross section to be smoother at large z than the charged-pion equivalent, giving easier access to partonic interpretation.

The advantage of SIDIS π° electroproduction is the reduced nucleon resonance contribution allowing access to larger z values in partonic interpretation.

E. Fragmentation Functions

Due to the lack of a priori calculations within QCD of the fragmentation process, embodying the long-range dynamics of confinement, one typically resorts to a parameterization in terms of fragmentation functions [47]. Fragmentation functions are similar as parton distribution functions universal, *i.e.*, process independent, with their dependence on the scale Q^2 well-known in terms of QCD evolution. In general, the fragmentation functions are, for the in the valence quark region most copious up and down quarks, assumed to not depend on quark flavor. Beyond the possibility to be flavor dependent, an additional complication is that one can have favored and unfavored fragmentation functions, D^+ and D^-, respectively, that refer to the case where the electro-produced meson contains the same flavor as the struck quark or not.

With the assumptions of factorization, isospin symmetry and charge conjugation (and neglecting heavy quarks in the valence-quark region), the cross sections of $\pi^\pm$ production on protons and neutrons at fixed Q^2 can be presented as:

$$
\begin{aligned}
{\sigma_p}^{\pi^+}(x,z) &\propto 4u(x)D^+(z) + d(x)D^-(z) + 4\bar{u}(x)D^-(z) + \bar{d}(x)D^+(z) \\
{\sigma_p}^{\pi^-}(x,z) &\propto 4u(x)D^-(z) + d(x)D^+(z) + 4\bar{u}(x)D^+(z) + \bar{d}(x)D^-(z) \\
{\sigma_n}^{\pi^+}(x,z) &\propto 4d(x)D^+(z) + u(x)D^-(z) + 4\bar{d}(x)D^-(z) + \bar{u}(x)D^+(z) \\
{\sigma_n}^{\pi^-}(x,z) &\propto 4d(x)D^-(z) + u(x)D^+(z) + 4\bar{d}(x)D^+(z) + \bar{u}(x)D^-(z),
\end{aligned}
\tag{11}
$$

with D^+ and D^- the favored and unfavored fragmentation functions defined as $D^+ = D_u^{\pi^+} = D_d^{\pi^-}$, and $D^- = D_u^{\pi^-} = D_d^{\pi^+}$, respectively.

In general, the SIDIS charged-pion electroproduction cross sections, including their ratios, will both depend on the favored and unfavored fragmentation functions, or their respective ratios. However, it is an assumption that only two fragmentation functions are needed for charged pions from valence quarks. In contrast, the neutral pion plays a different role due to its specific quark substructure, and the SIDIS neutral-pion electroproduction cross section will be related to the average of the two (D^+ and D^-) fragmentation functions. A similar result, under the assumption of flavor independence of the fragmentation functions, would follow from the often-used relation $\sigma^{\pi^\circ}(x,z) = [\sigma^{\pi^+}(x,z) + \sigma^{\pi^-}(x,z)]/2$. Inclusion of the π° final state to charged-pion data analysis allows for an important additional consistency check on the assumption that only two fragmentation functions are needed for charged pions.

The advantage of SIDIS π° electroproduction is the proportionality to an average fragmentation function.

F. The Problem Child: d/u Ratio

The measured cross sections or yields for $\pi^\pm$ production on the proton and deuteron can in the quark-parton model be directly used to form relations in terms of the u_v and d_v valence quark distributions:

$$
\begin{aligned}
{\sigma_p}^{\pi^+} - {\sigma_p}^{\pi^-} &\propto (D^+ - D^-)(4u_v - d_v) \\
{\sigma_d}^{\pi^+} - {\sigma_d}^{\pi^-} &\approx ({\sigma_p}^{\pi^+} - {\sigma_p}^{\pi^-}) + ({\sigma_n}^{\pi^+} - {\sigma_n}^{\pi^-}) \\
&\propto (D^+ - D^-)(3u_v + 3d_v),
\end{aligned}
\tag{12}
$$

where $u_v = u - \bar{u}$, and $d_v = d - \bar{d}$. Of course, only the full parton distribution u (and d) is physical, but at intermediate to large x, $x > 0.3$, sea quark contributions are small and it is common to consider valence quark distributions only in this region.

The d_v/u_v ratio can be directly extracted from a specific combination of the measured proton and deuteron $\pi^\pm$ cross sections as follows:

$$
R_{pd}^-(x) = \frac{\sigma_p^{\pi^+}(x,z) - \sigma_p^{\pi^-}(x,z)}{\sigma_d^{\pi^+}(x,z) - \sigma_d^{\pi^-}(x,z)} = \frac{4u_v(x) - d_v(x)}{3[u_v(x) + d_v(x)]},
\tag{13}
$$

from which one finds

$$
d_v/u_v = (4 - 3R_{pd}^-)/(3R_{pd}^- + 1).
\tag{14}
$$

Studying the x and z (and $P_{h\perp}$) dependencies of R_{pd}^- and d_v/u_v thus provides an excellent test of the validity of the high-energy factorized view of the SIDIS process, and the various assumptions made.

The ratio of d_v/u_v from E00-108 is shown in Fig. 4, both as a function of x at z=0.55 (top panel), and as a function of z at x=0.32 (bottom panel). The ratios extracted from our SIDIS data are also compared to WA-21/25 data from neutrino and anti-neutrino deep inelastic scattering off proton targets (solid squares) [48], and to ratios extracted from forward hadron production data from the European Muon Collaboration (open squares) [3]. The shaded bands on both panels represent the values (including their present uncertainties) as calculated from Eq. 13 using CTEQ parton distribution functions [17].

The experimentally extracted ratios appear somewhat low as compared to the quark-parton model expectations using the CTEQ parton distributions, but within 2σ uncertainties. A global fit of the E00-108 data

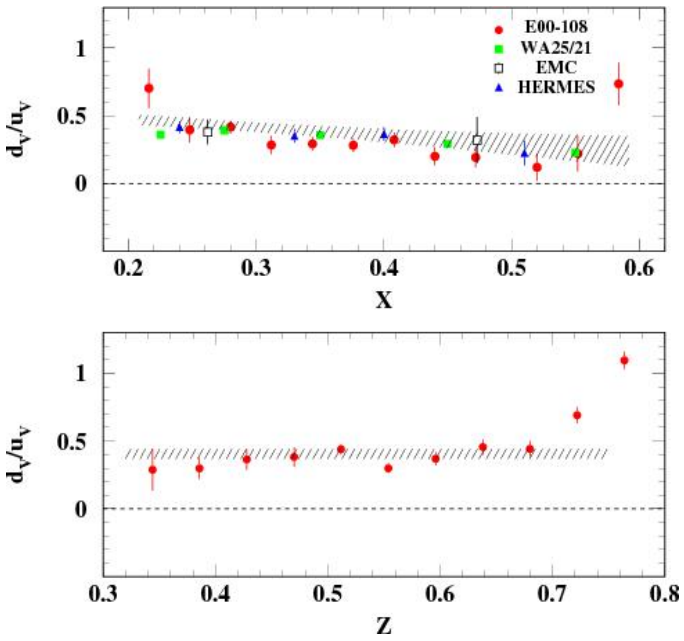

FIG. 4: (Color online) Top panel: The ratio of valence quarks d_v/u_v as a function of x at z=0.55. Solid circles are our data from E00-108 experiment (at $P_{h\perp} \approx 0$) after events from ρ decay are subtracted. Solid and open squares represent data from WA-21/25 [48] and EMC [3]. Solid triangle symbols are HERMES data [5] integrated over the $0.2 < z < 0.7$ range. Bottom panel: The ratio of valence quarks d_v/u_v as a function of z at x=0.32. Solid circles are our data from E00-108 after events from diffractive ρ decay are subtracted. The shaded bands on both panels reflect the values of and uncertainties in this ratio using CTEQ parton distribution functions, based on Eq. 13 [17].

folding in the $P_{h\perp}$ dependence (at $x = 0.32$ and $z = 0.55$ *only*), **and** assuming possible different (gaussian) widths of favored and unfavored, up and down transverse momentum dependencies, finds the ratio $d/u = 0.39 \pm 0.03$ (at $x = 0.30$) to be in agreement with the LO GRV98 fit for valence quarks (about 0.40) [1]. The E00-108 data (at $P_{h\perp} \approx 0$) are also in good agreement with previous extractions of WA21/25 and EMC, with vastly different techniques. Note that for these comparisons, one should not only take into account experimental systematic uncertainties, but also possible biases due to various assumptions in low-energy factorization and symmetry in fragmentation functions, etc., in the data interpretation of the presented E00-108 experiment. Nonetheless, at appearance the agreement is good, within the stated assumptions. This possibly points to the applicability of the assumed factorization and access to the quark-parton model in relatively low-energy SIDIS data, consistent with the findings in Ref. [16].

The possible undershoot as compared to CTEQ parton distribution function expectations as function of x can be further investigated by looking for the dependence on z of the measured ratios at a fixed value of x (= 0.32). If isospin symmetry between favored (D^+) and unfavored (D^-) fragmentation functions of light quarks (u and d) and anti-quarks ($\bar{u}$ and $\bar{d}$) breaks down ($D_u^{\pi^+} \neq D_{\bar{u}}^{\pi^-} \neq D_{\bar{d}}^{\pi^-} \neq D_{\bar{d}}^{\pi^+}$ and $D_u^{\pi^-} \neq D_{\bar{u}}^{\pi^+} \neq D_d^{\pi^+} \neq D_{\bar{d}}^{\pi^-}$), the ratios of Eq. 13 may contain additional z-dependent factors, related to asymmetries between the fragmentation functions. Thus, a dependence of the extracted "d_v/u_v ratio" on z will be a good indication for a breakdown of the symmetry assumptions, or of the factorized formalism. Indeed, one can witness in the bottom panel of Fig. 4 a sharp increase of the extracted d_v/u_v ratio at $z > 0.7$. This is likely not surprising as $z > 0.7$ corresponds in E00-108 kinematics to missing mass $M_x^2 < 2.5$ GeV^2), where *e.g.* the Δ- and higher-resonance contributions become dominant.

Below $z \approx 0.7$, the extracted d_v/u_v ratio is found to be reasonably independent of z, within the uncertainties of the data. On average, the data is again somewhat low as compared to the quark-parton model expectations based upon CTEQ parton distribution functions, similar as was found in the x-dependence of this ratio. Even if overall the data seem to point to the applicability of factorization and a partonic interpretation,

one can also play devil's advocate and wonder why the SIDIS data tend to undershoot the CTEQ parton model expectations if viewed as a whole (as function of x and z). The extracted d_v/u_v ratio tends to be very sensitive to the applicability (or not) of the assumed (x, z) factorization. Even more, unreleased SIDIS data of the HERMES collaboration (at larger energies) also point to potential pitfalls in the extraction of d_v/u_v. Hence, this warrants a thorough systematic study of the basic SIDIS pion electroproduction cross sections, *including* the π°, as a quantification of such factorization (at JLab energies). High statistics and precision cross section data will be of importance of such a study, following in the footsteps of E00-108.

IV. EXPERIMENT

We propose to measure basic cross sections of the semi-inclusive π° electroproduction process off a proton target, at small transverse momentum (scale $P_{h\perp} \approx \Lambda$). These neutral-pion measurements will provide crucial input towards our validation of the basic SIDIS framework and data analysis at JLab energies, explicitly in terms of validation of anticipated (x, z) factorization.

In this experiment we plan to make coincidence measurements between scattered electrons in the existing HMS and photons from π° decay in a Neutral Particle Spectrometer (NPS) using a $PbWO_4$ calorimeter. A detailed description of this setup, envisioned to be common for experiments requiring spectrometer-level precision and detecting neutral particles such as γ and π°, is given in [2] and also appended to this proposal. The NPS will detect photons corresponding to π° electroproduction close to the direction of $\vec{q}$ (parallel kinematics). These events correspond to θ_{π° near zero degrees, although, as will be shown later, we will have full (sufficient) coverage over ϕ_{π° up to transverse momentum of $P_{h\perp}$=0.3 (0.4) GeV and thus potentially eliminate any dependence on the interference terms.

We intend to perform all measurements on a hydrogen target, apart from the necessary (but short) Al "dummy" measurements for target wall subtraction. The experiment will use an 11-GeV beam energy to map a region in Bjorken x between 0.2 and 0.6, in z between 0.4 and 0.8, and in θ_{pq} to cover a range in $P_{h\perp}$ up to 0.4 GeV. To better constrain the possible (x, z) entanglement, we plan to measure over a range in Q^2 for *fixed* value of $x = 0.36$, while still varying z. All kinematics are compatible with a companion DVCS/DVNP proposal, and potentially part of one run group, a novelty within Hall C.

A. Choice of Kinematics

We plan to map the semi-inclusive neutral-pion electroproduction process off the proton target in a (x, Q^2) phase space compatible with the measurements approved for (unpolarized) semi-inclusive charged-pion electroproduction as approved in E12-09-017 and E12-09-002 in Hall C, but also E12-06-112 in Hall B. The HMS spectrometer setting (with the choice of 11 GeV beam energy) will determine the (x, Q^2) of the specific kinematics, for this proposal ranging between $x = 0.2$ and 0.6. The large solid angle (25 msr) and full momentum acceptance of the NPS will then allow to map the z, and $P_{h\perp}$ dependence, typically for a range of z between 0.4 and 0.8 and a range of $P_{h\perp}$ up to 0.3-0.4 GeV. We will measure the semi-inclusive neutral-pion electroproduction yields over the range in z and θ_{pq} for six kinematics in (x, Q^2), labeled $A - F$ (see Table III and IV). Figure 5 shows the accessible (x, Q^2) phase space for 12 GeV experiments in Hall C for exclusive and semi-inclusive kinematics, with the specific kinematics added where charged-pion SIDIS data are anticipated and neutral-pion SIDIS data from this proposal. The minimum laboratory angle of HMS is 10.5°. The minimum central laboratory angle for SHMS, or for NPS, will be 5.5°, with phase space extending down to ∼4°. In that sense, the (x, Q^2) phase space accessible in Hall C for deep exclusive and/or semi-inclusive reactions includes that of other Halls. For the first kinematics, at $(x,\ Q^2) = (0.20,\ 2.00\ \text{GeV}^2)$, we will park the HMS at 10.5° and benefit from the ≈3° angular acceptance of HMS to cover the nominal 10.27° scattering angle. The NPS angles in this proposal are 7.93° or larger, well beyond the envisioned smallest-angle of NPS, also alleviating backgrounds. The range in z while $M_x^2 > 2.5\ \text{GeV}^2$ is up to about $z = 0.7$-0.8. Given that the nucleon resonance contributions for

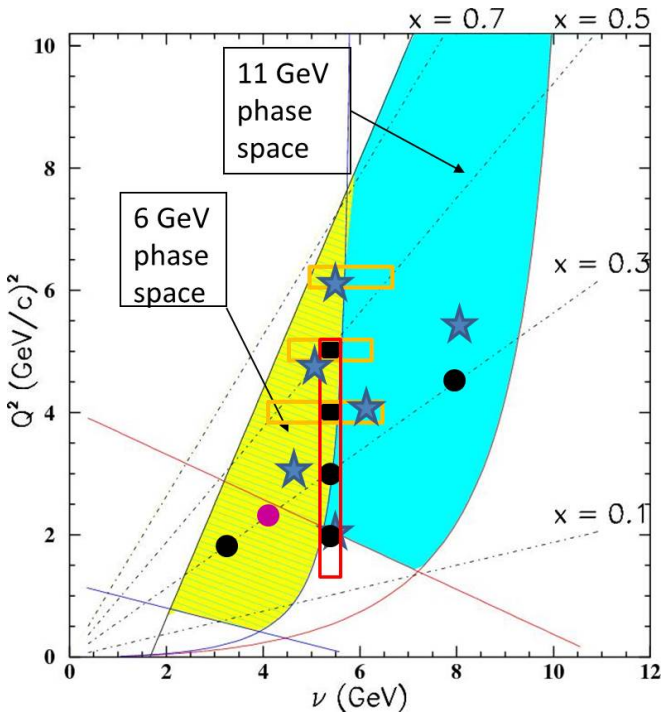

FIG. 5: Q^2 *versus x phase space available for semi-inclusive (or exclusive) coincidence experiments in Hall C at 11 GeV using the HMS and either the SHMS or the envisioned NPS. The stars indicate kinematics of proposed semi-inclusive* π° *production experiment. Other symbols indicate kinematics of the E00-108 (magenta circle), E12-09-017 (black circles), E12-06-104 (red box), E12-09-002 (yellow boxes) experiments.*

TABLE III: Kinematic settings, with HMS providing the electron spectrometer and NPS the neutral-pion spectrometer.

Kinematics	E (GeV)	E' (GeV)	θ_e (deg)	W^2 (GeV^2)	θ_γ (deg)	q_γ (GeV)	x	Q^2 (GeV^2)	z
A	11.0	5.67	10.27	8.88	10.57	5.513	0.20	2.0	0.4−0.8
B	11.0	6.56	11.70	6.21	16.20	4.767	0.36	3.0	0.5−0.8
C	11.0	5.08	15.38	7.99	12.44	6.250	0.36	4.0	0.4−0.8
D	11.0	2.86	24.15	10.66	7.93	8.472	0.36	5.5	0.3−0.8
E	11.0	5.88	15.65	5.68	16.57	5.565	0.50	4.8	0.4−0.8
F	11.0	5.67	17.84	4.88	17.23	5.865	0.60	6.0	0.4−0.8

$ep \to e'\pi^\circ\Delta^+$ are reduced as compared to $ep \to e'\pi^-\Delta^{++}$, the $M_x^2 > 2.5$ GeV^2 constraint may be relaxed.

In Fig. 6 we illustrate the $(P_{h\perp}, \phi)$ coverage for the various kinematics A-F. Excellent coverage in ϕ is obtained up to $P_{h\perp}$ of 0.3 GeV, and good/sufficient coverage up to $P_{h\perp} = 0.4$ GeV, to potentially remove any sensitivity to interference structure functions in SIDIS kinematics by integration, or alternatively determine $\cos(\phi)$ or $\cos(2\phi)$ moments, also of relevance for the E12-06-112 experiment in Hall B aiming at such moments up to large $P_{h\perp}$. In the appendix we have included the general kinematics overview Table VI of the companion proposed DVCS/DVNP experiment. We have added one row in the bottom to clarify what the proposed SIDIS kinematics A-F correspond to. SIDIS data would be accumulated simultaneously with the proposed DVCS/DVNP experiment. We note that the exact distance of the calorimeter is still under discussion, and is linked to the final sweeping magnet design. For SIDIS, we have assumed a generic distance of 4 meters, which works well with the present magnet design under discussion. The shorter distance of 3 meters would also benefit the SIDIS experiments and give somewhat larger $P_{h\perp}$ coverage, but will require a revisit of the magnet design as presently under consideration. For the NPS angles required for the SIDIS kinematics, this seems possible.

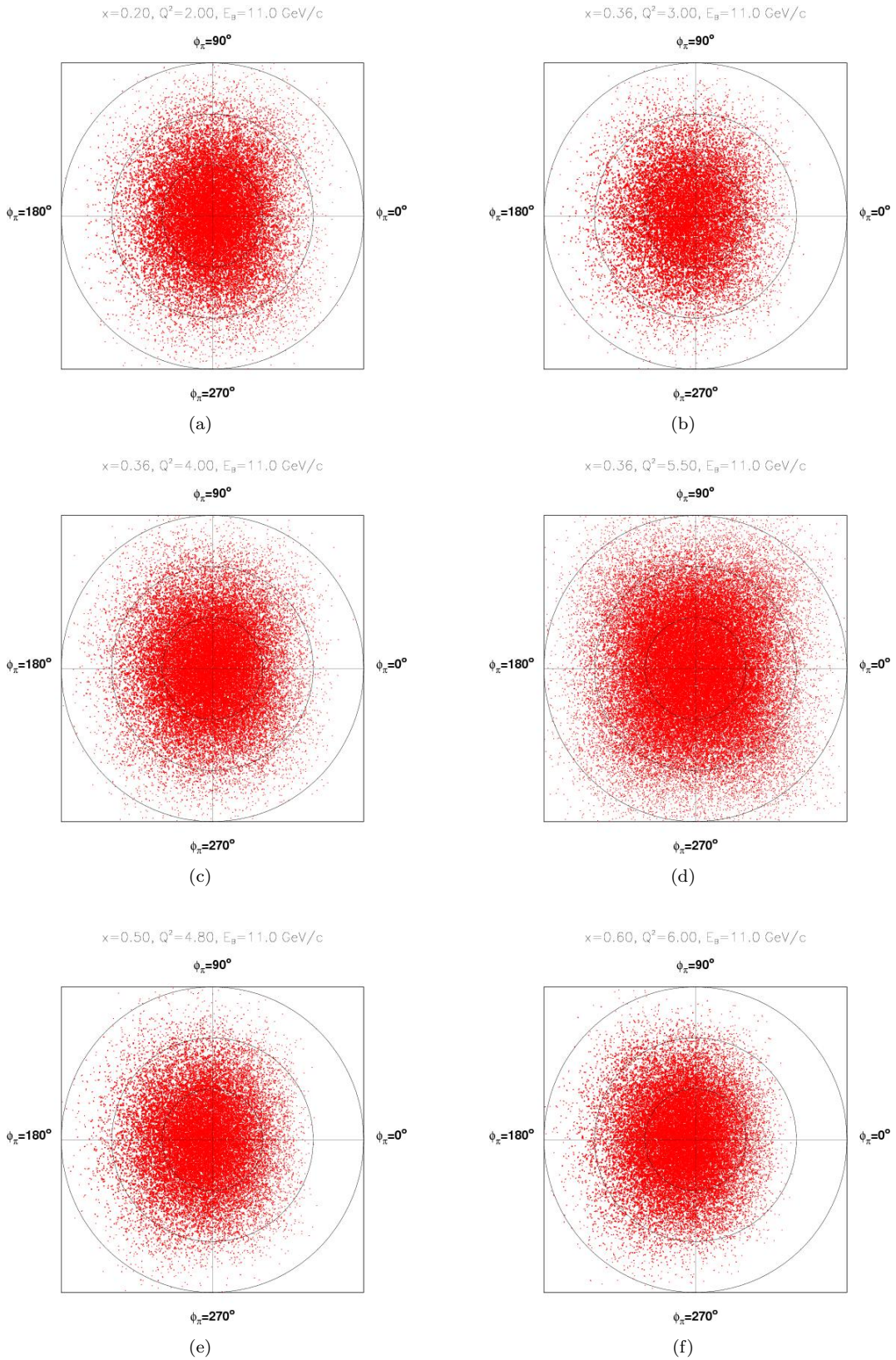

(a) (b) (c) (d) (e) (f)

FIG. 6: Coverage of proposed measurements in transverse momentum $P_{h\perp}$ and azimuthal angle ϕ. The plots are for the kinematics (a):($x,\ Q^2$) = (0.20, 2.00 GeV^2); (b):($x,\ Q^2$) = (0.36, 3.00 GeV^2); (c):($x,\ Q^2$) = (0.36, 4.00 GeV^2); (d):($x,\ Q^2$) = (0.36, 5.50 GeV^2); (e):($x,\ Q^2$) = (0.50, 4.80 GeV^2) and (f):($x,\ Q^2$) = (0.60, 6.00 GeV^2) . The circles indicate $P_{h\perp}$ = 0.2, 0.4, and 0.6 GeV, respectively.

TABLE IV: Kinematic settings and expected coincidence counts within $\triangle z$=0.1 bins for the Semi-Inclusive $(e, e'\pi^\circ)X$ production measurements. The NPS is positioned along the virtual photon direction as caluclated from central kinematics. The beam energy is 11 GeV. Beam current is assumed to be 1 μA, and the target is assumed to be 10 cm LH2 for the rate estimates. Rates are given in kilo-counts per hour, with the "detected" column taking into account the geometric π° detection effficiency.

Kinematics	E (GeV)	E' (GeV)	θ_e (deg)	x	Q^2 (GeV^2)	W (GeV)	θ_γ (deg)	q_γ (GeV/c)	$\pi^\circ - eff$ (%)	z	k-counts/h expected	k-counts/h detected
A	11.0	5.67	10.27	0.20	2.00	2.98	10.57	5.513	1.0	0.30	26.11	0.261
									9.3	0.40	29.89	2.780
									19.9	0.50	30.37	6.109
									29.5	0.60	27.23	8.033
									38.0	0.70	21.15	8.037
									45.4	0.80	12.37	5.616
B	11.0	6.56	11.70	0.36	3.00	2.49	16.21	4.767	0.0	0.30	10.87	0.054
									3.0	0.40	12.66	0.380
									11.1	0.50	13.06	1.450
									19.9	0.60	11.83	2.354
									28.0	0.70	9.30	2.604
									35.3	0.80	5.99	2.114
C	11.0	5.08	15.38	0.36	4.00	2.83	12.44	6.250	3.0	0.30	3.92	0.118
									14.1	0.40	4.45	0.627
									25.5	0.50	4.46	1.137
									35.3	0.60	3.93	1.387
									43.8	0.70	3.00	1.314
									51.1	0.80	1.86	0.950
D	11.0	2.86	24.14	0.36	5.50	3.26	7.93	8.472	15.6	0.30	0.68	0.106
									30.6	0.40	0.73	0.223
									42.7	0.50	0.70	0.299
									52.8	0.60	0.58	0.306
									61.0	0.70	0.42	0.256
									68.2	0.80	0.25	0.171
E	11.0	5.88	15.65	0.50	4.80	2.38	16.57	5.565	0.5	0.30	2.10	0.011
									7.7	0.40	2.45	0.189
									17.9	0.50	2.47	0.442
									27.3	0.60	2.21	0.603
									35.7	0.70	1.71	0.610
									43.0	0.80	1.08	0.464
F	11.0	5.67	17.84	0.60	6.00	2.21	17.23	5.865	1.0	0.30	0.75	0.008
									9.3	0.40	0.86	0.080
									20.0	0.50	0.87	0.174
									29.6	0.60	0.77	0.228
									38.0	0.70	0.59	0.224
									45.4	0.80	0.37	0.168

B. Physics Singles Rates and Physics Backgrounds

Singles rates from (e, π°) and (e, e') can result in accidental coincidences which are a source of background for the measurement. However, as compared to the magnetic spectrometer setup planned for various $(e, e'\pi^\pm)$ experiments in Hall C (E12-06-104, E12-07-105, E12-09-002, E12-09-017) the beam current assumption ($\sim$ few μA) is modest as compared to the more typical >50 μA of the mentioned experiments, with similar length cryogenic targets. This implies a negligible accidental coincidence rate of about 2-10%, which can be easily

subtracted.

The singles rate in the HMS is in fact expected to be, while assuming here a 10 μA beam current, less than 12 kHz. Hence, projected rates for the HMS are low and are well within the operating parameters of previous HMS experiments. In this experiment, the π/e ratio in the HMS is never larger than ∼100:1, even without reducing this ratio at the hardware trigger level. The electron will be identified using the lead-glass calorimeter in combination with the gas Cherenkov. These modest rates and favorable π/e ratios allow us to always record the inclusive ^{1}H(e,e$'$) singles, which allows for reduced uncertainties in the SIDIS data analysis for which ratios of (e,e$'\pi^\circ$) and (e,e$'$) yields are relevant, reducing uncertainties.

The singles rates in the neutral-pion detector are dominated by background. This was simulated and is discussed in detail in a dedicated writeup for the NPS, see Ref. [2] and also appended to this proposal.

We have chosen a liquid hydrogen target with a length of 10 cm. This means that the target end windows will be in the acceptance of the spectrometers (HMS and NPS) in all configurations, and the background subtractions are necessary. Background events from the target end windows will be measured in "empty" target runs. The Hall C empty target consists of two thin Aluminum pieces separated by a length equivalent to the cryogenic target length. However, the empty target is thicker by a factor of 6-7 relative to the target cell walls, a thickness chosen to make the radiation lengths of LH2 (plus windows) and these "empty" targets about equivalent. The thicker target allows for a more rapid accumulation of counts for these background subtraction measurements. These short measurements are implicitly included in the beam time request.

C. Systematic Uncertainties

The estimated systematic uncertainties for the $(e, e'\pi^\circ)$ SIDIS reaction are listed in Table V. These are largely based on the previous experience with the HMS+SOS spectrometer pair in Hall C, and we benefit from the well-understood HMS that will determine the (x, Q^2) kinematics allowing for a precision similar as in Hall C's longitudinal-transverse cross section separation program. In fact, in comparison to the 6-GeV coincidence measurements in which the electron was detected in the SOS, we expect some improvements in the contributions to the systematic uncertainty. For example, the HMS acceptance is much flatter than the SOS acceptance. The neutral-pion acceptance is fully given by geometry and not prone to magnetic field knowledge at all. Tracking efficiency knowledge in the HMS is expected to be excellent at the low rates anticipated in this experiment. In the case of π° detection, the calorimeter performance is expected to be comparable to the one in the PRIMEX-II experiment, with detailed understanding.

Some uncertainties will be larger than, for instance, those projected for the charged-pion L/T separations in electroproduction and the pion form factor measurements at 12 GeV. First of all, the beam current can be as low as 1 μA. We conservatively assume a 2% scale uncertainty (this may be reduced to 1% with a lead-tungsten calorimeter under consideration), and a 0.5% relative measurement of the collected beam charge. Of course, we note that in the semi-inclusive data analysis only the ratio of $(e, e'\pi^\circ)$ and (e, e') yields is relevant, with absolute beam current knowledge dropping out. This is why it is important to accumulate in the data acquisition the HMS (e,e$'$) singles in addition to the (e,e$'\pi^\circ$) SIDIS coincidence events.

Secondly, we plan to use the HMS spectrometer up to a momentum of 6.6 GeV/c, some 10% below its maximum design momentum of 7.3 GeV/c. Data taking at a 6-GeV Jefferson Lab has shown an excellent and stable performance and detailed understanding of this for HMS momentum up to $\sim$ 5.5 GeV/c. Some saturation effects are anticipated in the magnetic performance equivalent to a central momentum of 6.6 GeV/c. The anticipated behavior in the HMS quadrupole magnets has been mapped through rotating-coil measurements in the early 1990s, but exact implications for the understanding of the HMS optics and acceptance require data. Luckily, the implications are expected to be minor as compared to the magnetic field saturation effects one had to face with the SOS for the earlier 6-GeV precision L/T separation program in Hall C. Even more, we only plan to use the HMS at angles below 25° with a modest 10 cm long target, which essentially acts as a point target for HMS optics. Nonetheless, we have retained a 1% scale uncertainty in the understanding of the acceptance of the HMS for the (e,eπ°) cross sections. Note again that for the SIDIS analysis the ratios of (e,eπ°) to (e,e$'$)

TABLE V: *Estimated systematic uncertainties for the π° cross section measurements based on previous Hall C experiments. We have remained separation between point-to-point uncertainties (pt-to-pt), relevant for separated structure functions, and scale uncertainties. The scale uncertainties are for the (e,eπ°) cross sections, not for the ratios of (e,eπ°) to (e,e$'$) yields that are more relevant for the SIDIS analysis. It is important to realize that the HMS is a very well understood magnetic spectrometer which will be used in modest requirements (beyond the momentum), defining the (x, Q^2) kinematics well. The pt-to-pt (scale uncertainties) for radiative corrections and Monte Carlo model are 1% (2%) and 0.2% (1%), and should be added in quadrature in the total.*

Source	pt-to-pt (%)	scale (%)
Acceptance	0.4	1.0
Electron PID	<0.1	<0.1
π° efficiency [a]	1.0	1.0
Electron tracking efficiency	0.1	0.5
Charge	0.5	2.0
Target thickness	0.2	0.5
Kinematics	0.3	<0.1
Total (including rad, mod)	1.6	3.4
Total	1.2	2.5

[a]includes combinatoric background

yields are more relevant, reducing the sensitivity to systematic uncertainties due to HMS understanding.

Thirdly, some variation of the gain of the PMTs, and degradation of the $PbWO_4$ crystals during the experiment is anticipated. To minimize variation in the PMT gains at high rates (as observed in PRIMEX) we will use active bases with built-up pre-amplifiers which powered from a high-voltage division chain [49]. This active base will allow for operating the PMTs at lower voltages and lower anode currents, with gain stability better than ∼1% for the rates up to ∼1.5 MHz. Nevertheless we have included a projected 1% nonlinearity in gain leading to the projected 1% of "PID" (π° PID and efficiency) in Table V. This is far more conservative than the achieved knowledge from the PRIMEX-II experience.

Lastly, well-established models for separated pion electroproduction cross sections above the resonance region do not exist, and there will thus be equivalent uncertainty in the radiative correction estimates. Even if reduced due to the less prominent role of the nucleon resonances in the π° channel (as compared to π^+), this may be the largest single systematic uncertainty for the proposed experiment. This can be reduced through further data accumulation for this process with 12-GeV experiments.

V. SUMMARY AND BEAM TIME REQUEST

We request a total of 25 days of beam time to measure basic cross sections for semi-inclusive electroproduction of neutral pions from a proton target, to a level of 3% precision. The cross section measurements will cover a range compatible with the approved charged-pion basic cross section program, $0.2 < x < 0.6$, $2 < Q^2 < 6$ GeV^2, $0.4 < z < 0.8$, and $P_{h\perp} < 0.4$ GeV, and will provide a firm basis to validate our understanding of the (x, z) factorization in the SIDIS framework at a 12-GeV JLab. This will shed light on various potential analysis pitfalls, and provide the foundation for a solid interpretation of any semi-inclusive deep inelastic scattering data within a partonic description.

We plan to perform such (e,e$'\pi^\circ$) coincidence measurements utilizing the well-understood HMS with a new Neutral-Pion Spectrometer facility. Inclusive (e,e$'$) yields in HMS will be accumulated simultaneously to reduce systematic uncertainties in the SIDIS analysis. We request a polarized electron beam to add the possibility to determine single-spin asymmetries from these measurements.

This proposal is part of a rungroup with a companion DVCS/DVNP proposal, and thus provides a unicum

within Hall C. The 25 days of beam time request are fully compatible with the DVCS/DVNP companion proposal, and assume a beam current ranging from 1 to ∼30 μA, and a 10 cm LH2 target, with a base beam energy of 11.0 GeV. The days of beam time request are driven by the companion DVCS/DVNP proposal and assume for kinematics A-F one day, one day, three days, five days, five days, and ten days, respectively. For this SIDIS proposal this will render 10K events for each z bin, even at a conservative beam current of 1 μA.

[1] R. Asaturyan *et* al., Phys. Rev. C **85** (2012) 015202.

[2] Neutral Particle Spectrometer Facility in Hall C. Proposal to Jefferson Lab PAC40; https://hallcweb.jlab.org/experiments/PAC40/nps.pdf, Contact person T. Horn.

[3] J. Ashman *et al.*, Phys. Lett. **B 206**, 364 (1988), Nucl. Phys. **B 328**, 1 (1989).

[4] P. L. Anthony *et al.*, Phys. Lett. **B 458**, 529 (1999); **B 463**, 339 (1999); **B 493**, 19 (2000).

[5] A. Airapetian *et al.*, Phys. Lett. **B 404**, 383 (1997); **B 444**, 531 (1998); **B 442**, 484 (1998).

[6] J. Adams *et al.*, Phys. Rev. Lett. **92**, 171801 (2004); S. S. Adler *et al.*, Phys. Rev. Lett. **91**, 241803 (2003).

[7] A. Accardi, T. Hobbs, and W. Melnitchouk, JHEP 0911 (2009) 084.

[8] F.E. Close and W. Melnitchouk, Phys. Rev. C **79** (2009) 055202

[9] J. T. Dakin, G. J. Feldman, F. Martin, M. L. Perl, and W. T. Toner, Phys. Rev. Lett. **31**, 786 (1973).

[10] M. Stratmann and W. Vogelsang, Nucl. Phys. **B496**, 41 (1997); D. de Florian and R. Sassot, Phys. Rev. D **56**, 426 (1997).

[11] A. S. Raskin and T. W. Donnelly, Ann. Phys. (N.Y.) **191**, 78 (1989).

[12] J. Binnewies, B. A. Kniehl, and G. Kramer, Phys. Rev. D **52**, 4947 (1995).

[13] E. L. Berger, Nucl. Phys. **B85**, 61 (1975).

[14] E. L. Berger, Proc. of the Workshop on Electronuclear Physics with Internal Targets, Stanford, CA, January 5-7, 1987.

[15] P. J. Mulders, in: R. G. Milner (Ed.), EPIC 2000: Proceeding of the 2nd Workshop on Physics with an Electron Polarized Light Ion Collider, Cambridge, MA, 2000; arXiv:hep-ph/0010199v1, 2000.

[16] T. Navasardyan *et al.*, Phys. Rev. Lett. **98** (2007) 022001.

[17] H. L. Lai, J. Huston, S. Kuhlmann, J. Morfin, F. Olness, J. F. Owens, J. Pumpin and W. K. Tung, Eur. Phys. J. C **12**, 375 (2000).

[18] X. Ji, J.-P. Ma, F. Yuan, Phys. Lett. **B597**, 299 (2004).

[19] P.J. Mulders and R.J. Tangerman, Nucl. Phys. **B461**, 197 (1996).

[20] A. Bachetta, M. Diehl, K. Goeke, A. Metz, P.J. Mulders, and M. Schlegel, JHEP **0702**, 093 (2007).

[21] M. Anselmino *et al.*, Eur. Phys. J. **A47**, 35 (2011).

[22] R.N. Cahn, Phys. Lett. **B78**, 269 (1978); Phys. Rev. **D40**, 3107 (1989)

[23] M. Anselmino, M. Boglione, U. D'Alesio, A. Kotzinian, F. Murgia and A. Prokudin, AIP Conf. Proc. **792**, 981 (2005) [arXiv:hep-ph/0507157]; M. Anselmino, M. Boglione, A. Prokudin and C. Turk, Eur. Phys. J. A **31**, 373 (2007) [arXiv:hep-ph/0606286]; M. Anselmino *et al.*, Phys. Rev. **D71** (2005) 074006; M. Anselmino, M. Boglione, A. Prokudin, and C. Turk, Eur. Phys. J. **A31** (2007) 373.
[24] A. Airapetian *et al.*, Phys. Rev. D **87** (2013) 012010.
[25] G. Sbrizzai *et al.*, J. Phys. Conf. Ser. **295** (2011), 012043; DIS2013 presentation (2013), see https://indico.cern.ch/contributionDisplay.py?sessionId=7&contribId=224&confId=184503.
[26] H. Mkrtchyan *et al.*, Phys. Lett. **B665** (2008) 20.
[27] M. Wakamatsu, Phys. Rev. **D79** (2009) 094028.
[28] P. Schweitzer, T. Teckentrup, and A. Metz, Phys. Rev. D **81**, 094019 (2010).
[29] M. Osipenko *et al.*, Phys. Rev. D **80**, 032004 (2009).
[30] T. Sjostrand, S. Mrenna, and P. Z. Skands, JHEP 05 (2006) 026; T. Sjostrand, L. Lonnbland, S. Mrenna, and P. Z. Skands, arXiv:hep-ph/0308153v1.
[31] P. Liebing, Ph.D. dissertation, University of Hamburg, 2004.
[32] C. Hadjidakis, Ph.D. dissertation, Institut de Physique Nucleaire Orsay, 2002.
[33] H. Avagyan (private communication).
[34] L. W. Mo and Y. S. Tsai, Rev. Mod. Phys. **41**, 205 (1969).
[35] R. Ent, B. Filippone, N. C. R. Makins, R. G. Milner, T. G. O'Neill and D. A. Wasson, Phys. Rev. C **64**, 054610 (2001).
[36] D. M. Koltenuk, Ph.D. thesis, University of Pennsylvania, 1999.
[37] D. Gaskell, Ph.D thesis, Oregon State University, 2001.
[38] I. Akushevich, A. Ilyichev, N. Shumeiko, A. Soroko, A. Tolkachev, Comp. Phys. Comm. **104**, 201 (1997).
[39] T. V. Kuchto and N. M. Shumeiko, Nucl. Phys. **B219**, 412 (1983).
[40] I. Akushevich and N. M. Shumeiko, J. Phys. G: Nucl. Part. Phys. **20**, 513 (1994).
[41] P. Brauel, T. Canzler *et al.*, Z. Physik C **3**, 101 (1979).
[42] H. P. Blok *et al.*, Phys. Rev. C **78**, 045202 (2008).
[43] V. Tadevosyan *et al.*, Phys. Rev. C **75**, 055205 (2007).
[44] T. Horn *et al.*, Phys. Rev. Lett. **97**, 192001 (2006).
[45] D. Drechsel, S. S. Kamalov, and L. Tiator, Nucl. Phys. **A645**, 145 (1999).
[46] I. Akushevich, N. Shumeiko, and A. Soroko, Euro. Phys. J. C **10**, 681 (1999).
[47] E. Garutti, Ph.D. Dissertatio, Amsterdam University (2003).
[48] G. Jones *et al.*, Z. Phys. C **62**, 601 (1994).
[49] V. Popov, H. Mkrtchyan, New potomultiplier active base for Hall C Jefferson Lab Lead Tungstate Calorimeter, NSSS2012-1098.

VI. APPENDIX

In this appendix we have included the general kinematics overview Table VI of the companion proposed DVCS/DVNP experiment. We have added one row in the bottom to clarify what the proposed SIDIS kinematics A-F correspond to. SIDIS data would be accumulated simultaneously with the proposed DVCS/DVNP experiment.

TABLE VI: DVCS Kinematics for Hall C. The incident and scattered beam energies are k and k', respectively. The calorimeter is centered at the angle $\theta_{\rm Calo}$, which is set equal to the nominal virtual photon direction. The front face of the calorimeter is at a distance $D_{\rm Calo}$ from the center of the target, and is adjusted to optimize multiple parameters: First to maximize acceptance, second to ensure sufficient separation of the two clusters from symmetric $\pi^0 \to \gamma\gamma$ decays, and third to ensure that the edge of the calorimeter is never at an angle less than 3.2° from the beam line. The last row indicates the kinematics that are used simultaneously for this proposal, corresponding to the total request of 25 days. Kinematics that would be of general interest to push the Q^2 range of SIDIS experiments, but beyond the scope of the presently considered JLab SIDIS program, are marked with a G-I.

	Energy Dependence at fixed (Q^2, $x_{\rm Bj}$)												Low-$x_{\rm Bj}$				High-Q^2		
$x_{\rm Bj}$	0.36					0.50			0.60				0.2				0.36	0.50	0.60
Q^2 (GeV)^2	3.0			4.0		3.4		4.8	5.1			6.0	2.0			3.0	5.5	8.1	10
k (GeV)	6.6	8.8	11	8.8	11	8.8	11	11	6.6	8.8	11	11	6.6	8.8	11	11	11		
k' (GeV)	2.2	4.4	6.6	2.9	5.1	5.2	7.4	5.9	2.1	4.3	6.5	5.7	1.3	3.5	5.7	3.0	2.9	2.4	2.1
$\theta_{\rm Calo}$ (deg)	11.7	14.7	16.2	10.3	12.4	20.2	21.7	16.6	13.8	17.8	19.8	17.2	6.3	9.2	10.6	6.3	7.9	8.0	8.0
$D_{\rm Calo}$ (m)	3	3	3	4	3	3	3	3	3	3	3	3	6	4	4	6	4	4	4
Days	1	2	1	1	3	3	2	5	5	1	5	10	1	1	1	1	5	5	12
SIDIS			B		C			E				F			A	G	D	H	I

We have chosen kinematics A-F of this proposal to be overlapping the approved unpolarized cross section and azimuthal asymmetry measurement phase space of SIDIS experiments in Hall C. Nonetheless, some additional kinematics could provide important information for possible later SIDIS studies where one pushes to the corners of allowable phase space (in Q^2) at a 12-GeV JLab. These kinematics are indicated as G, H, and I, with more information on coincidence rates given in Table VII. We would foresee to take parasitic SIDIS data in these kinematics might the proposed DVCS/DVNP experiment be (hopefully) approved, albeit at reduced statistics per z bin.

TABLE VII: Additional possible Kinematic settings (overlapping with other experiments) and expected coincidence counts within $\triangle z$=0.1 bins for the Semi-Inclusive $(e, e'\pi^\circ)X$ production measurements. Pions are along the virtual photon direction. The NPS is positioned along the virtual photon direction as caluclated from central kinematics. The beam energy is 11 GeV. Beam current is assumed to be 1 μA, and the target is assumed to be 10 cm LH2 for the rate estimates. Rates are given in kilo-counts per hour, with the detected column taking into account the geometric π° detection effficiency.

Kinematics	E (GeV)	E' (GeV)	θ_e (deg)	x	Q^2 (GeV^2)	W (GeV)	θ_γ (deg)	q_γ (GeV/c)	$\pi^\circ - eff$ (%)	z	k-counts/h expected	k-counts/h detected
G	11.0	3.01	17.32	0.20	3.00	3.59	6.28	8.179	14.6	0.30	3.59	0.524
									29.6	0.40	3.93	1.163
									41.8	0.50	3.78	1.580
									51.8	0.60	3.18	1.647
									60.2	0.70	2.31	1.391
									67.2	0.80	1.37	0.921
H	11.0	2.37	32.39	0.50	8.10	3.00	8.02	9.090	18.5	0.30	0.12	0.022
									33.6	0.40	0.13	0.044
									45.9	0.50	0.12	0.055
									56.0	0.60	0.10	0.056
									64.3	0.70	0.07	0.045
									71.3	0.80	0.04	0.029
I	11.0	2.12	38.24	0.60	10.00	2.75	7.99	9.428	19.9	0.30	0.03	0.006
									35.3	0.40	0.04	0.014
									47.6	0.50	0.03	0.014
									57.5	0.60	0.03	0.017
									65.7	0.70	0.02	0.013
									72.6	0.80	0.01	0.007

(Proposal to Jefferson Lab PAC 40)

Neutral Particle Spectrometer Facility in Hall C

May 5, 2013

A. Camsonne, R. Ent, P. Nadel-Turoński, S.A. Wood, B. Wojtsekhowski
Jefferson Lab, Newport News, VA 23606

A. Asaturyan, A. Mkrtchyan, H. Mkrtchyan, V. Tadevosyan, S. Zhamkochyan
A.I. Alikhanyan National Science Laboratory, Yerevan 0036, Armenia

M. Guidal, C. Munoz Camacho, R. Paremuzyan
Institut de Physique Nucleaire d'Orsay, IN2P3, BP 1, 91406 Orsay, France

I. Albayrak, M. Carmignotto, J. Dénes-Couto, N. Hlavin, T. Horn[1] F. Klein, B. Nepal
The Catholic University of America, Washington, DC 20064

C. Hyde, M.N.H. Rashad
Old Dominion University, Norfolk, Virginia

P. King, J. Roche
Ohio University, Athens, OH 45701

D. Day, D. Keller, O. Rondon
University of Virginia, Charlottesville, VA, USA

D. Hamilton
University of Glasgow, Glasgow, Scotland, UK

S. Sirca
University of Ljubljana, Ljubljana, Slovenia

[1] Contact person: hornt@jlab.org

Contents

I. INTRODUCTION

We plan to augment the capability of Hall C for precision cross section measurements of charged particles with a general-purpose and remotely rotatable neutral particle spectrometer (NPS). The proposed neutral particle detection system can be used in conjunction with Hall C's well-understood High-Momentum Spectrometer (HMS) for high-precision absolute cross section measurements at Jefferson Lab within the 12-GeV era [1] . It also facilitates from the wide range accessible with HMS, with an angle range between 10.5° and ∼80°, and a central momentum reach of up to 7.3 GeV/c. In coincidence, systematic point-to-point uncertainties of well below 2% are foreseen with this setup.

This neutral particle detection system is cantelevered of, or positioned on, the SHMS carriage to allow for two flexible remote-rotatable angle ranges from 5.5°-30°, and from 20°-60°, and consists of the following elements: i) a sweeping magnet; ii) a 25 msr $PbWO_4$-based neutral particle detector; iii) high voltage distribution bases with built-in amplifiers for operation in high-rate environments; iv) essentially deadtime-less digitizing electronics; v) a dedicated beam pipe to reduce backgrounds.

The facility will allow precision measurements requiring photon or neutral-pion detection in coincidence with the existing and well-understood Hall C High-Momentum Spectrometer to detect the scattered electrons (or recoiling protons). It can be used as photon detector for Deeply-Virtual Compton Scattering or Wide-Angle Compton Scattering reactions benefitting from the accessible range of HMS. It can also be used as neutral-pion detector, where the neutral pion will be detected by measurement of its $\gamma\gamma$ decay products in a dedicated neutral-pion detector.

To reduce electromagnetic backgrounds, we plan to use a conventional sweeping magnet, similar but with only ∼10% of the field requirements as the Horizontal-Bend magnet presently under construction for the new Hall C/SHMS to maintain access to small-angle ($\sim 5.5°$) $\pi°$ detection. Detailed background simulations show this setup safely allows for 2 μA beam current on a 10 cm long cryogenic LH2 target down to the very smallest NPS angles, and much higher luminosities at more backward angles.

II. EXPERIMENTAL SETUP

We propose to make a precision coincidence setup measuring charged particles (scattered electrons or recoiling protons) with the existing HMS and photons, either single photons or from the decay of neutral pions, in a neutral particle channel using a $PbWO_4$ calorimeter. A high luminosity spectrometer+calorimeter system like the HMS+$PbWO_4$ combination in Hall C is well suited for such measurements. The magnetic spectrometers benefit from relatively small point-to-point uncertainties, which are crucial for absolute cross section measurements such as those needed for meaningful L-T separations. In particular, the optics properties and the acceptance of the HMS have been studied extensively and are well understood in the kinematic range between 0.5 and 5 GeV, as evidenced by more than 200 L/T separations ($\sim$ 1000 kinematics) [2]. The position of the elastic peak has been shown to be stable to better than 1 MeV, and the precision rail system and rigid pivot connection have provided reproducible spectrometer pointing for about a decade.

A. NPS Facility Overview

We will construct a general-purpose and remotely rotatable NPS system for Hall C. A floor layout of the HMS and the proposed NPS system is shown in Fig. 1(a). This system consists of the following elements:

- A sweeping magnet providing 0.3 Tm field strength, with similar outer geometry as the Horizontal-Bend (HB) Magnet presently under construction for the SHMS but with conventional copper coils.
- A neutral particle detector consisting of 1116 $PbWO_4$ blocks (similar to the PRIMEX [3] experimental setup, see Fig. 1(b)) in a temperature controlled frame, comprising a 25 msr device at a distance of 4 meters.

- Essentially deadtime-less digitizing electronics to independently sample the entire pulse form for each crystal allowing for background subtraction and identification of pile-up in each signal. This is a major improvement over the existing PRIMEX apparatus.
- A new set of high voltage distribution bases with built-in amplifiers for operation in high-rate environments.
- Cantelevered platforms of the SHMS carriage, to allow for precise and remote rotation around the Hall C pivot of the full Neutral Particle Spectrometer, over an angle range between 5.5 and 30 degrees.
- A dedicated beam pipe with as large critical angle as possible to reduce backgrounds beyond the HB-type sweeping magnet.

To provide space for this sweeping magnet, the HB magnet for the SHMS needs to be removed. The HB adds a 3 degree horizontal pre-bend to the SHMS to allow reaching the smallest angles, as compared to an 18 degree vertical bend. Thus, it only provides a small perturbation to the SHMS optics, and as such removing and reinstalling the HB magnet does not impact the final SHMS optics understanding, given proper attention to alignment. In fact, the SHMS is in this sense comparable to the earlier SOS optics, where removing and properly reinstalling and realigning the SOS quadrupole did not imply additional optics understanding work beyond the standard sieve-slit calibration runs.

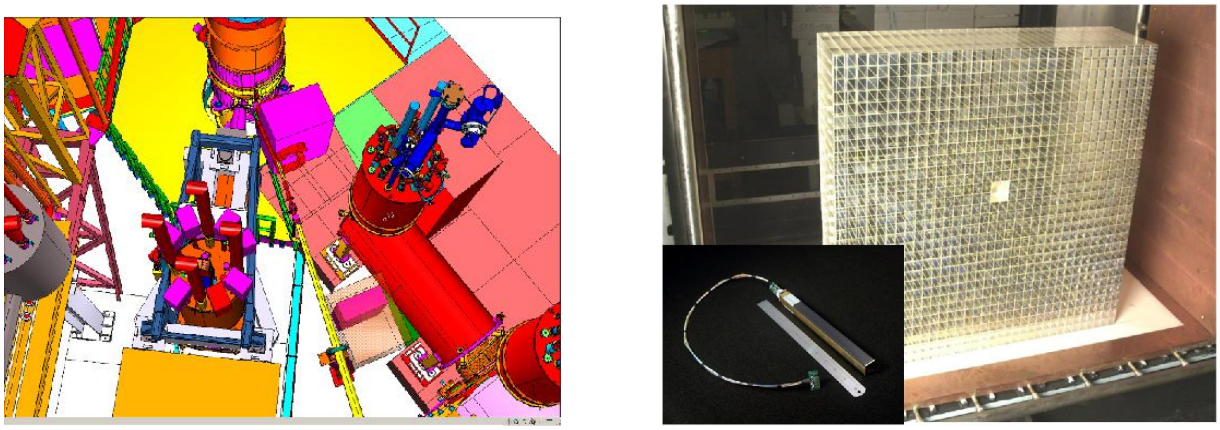

(a) (b)

FIG. 1: *(a)The NPS detector in Hall C. The cylinder at the top center is the (1 m diameter) vacuum chamber containing the 10 cm long liquid-hydrogen target. The long yellow tube emanating from the scattering chamber on the lower right is the downstream beam pipe. To the left of the beam pipe is the HMS. Only the liquid He and liquid N_2 lines for the large superconducting quadrupoles at the entrance to the spectrometer are clearly visible. To the right of the beam line, the first quadrupole of the SHMS and its cryogenic feed lines are shown. This spectrometer will be used for π° experiments as a carriage to support the $PbWO_4$ calorimeter (shown in its light-tight and temperature control box next to the beam line) and the associated sweep magnet. (b) The high resolution $PbWO_4$ part of the HYCAL [4] on which the present design is based.*

The sweeping magnet will be a conventional version of the HB magnet presently under construction, with copper coils to effectively use the full bore of such a magnet (35 by 36 cm^2). In sharp contrast to the superconducting HB magnet, which provides a field strength of 1.93 Tm, we only require a 0.3 Tm field to sweep away charged particles up to 300 MeV/c. This modest field requirement is well within the range of conventional magnet coils, alleviating the need for additional cryogenic and inner vacuum cans. The sweeping magnet design is matched to existing JLab power supplies and existing commercial conductors. The materials for the coil, a 24 m of copper conductor of dimension 0.5x0.5 in^2, including a 1/4 inch diameter water cooling channel, could be obtained from, for instance, Luvata-Finnland. The coil winding tools could be obtained through AES-Penn. The materials for the yoke steel could be obtained from vendors like Oakland Steel and would be purchased in slabs of 4" for easier machining in university machine shops. These magnet component vendors also supplied

the respective components for the Hall A PREX magnet. The estimated radiation dose at the location of the magnet (< 30,000 rem/hr) was folded into decisions for radiation hard resins and insulation systems.

The obvious advantage of using a sweeping magnet cloning the geometric properties of the HB magnet is that it has a relatively large bore, of 35 by 36 cm^2, and is designed from the start to reach small scattering angles without impacting the main electron beam. The effective gap for an HB-type magnet for neutral particle may be slightly reduced, as the coil assumes a 3 degree horizontal pre-bend for charged particles. Thus, if we assume a direct clone of the HB the effective gap for neutral particles (assuming symmetric acceptance around the detection angle) is reduced to about 30 by 36 cm^2. This problem likely gets alleviated for a conventional magnet but we have assumed the latter aperture for the rate estimates. We found that we can move the "HB-clone" sweeping magnet about 20 cm forwards as compared to the HB, such that the magnetic center is at a distance of 1.57 m from the pivot. This then constitutes a solid angle of 25.5 msr, with ∼146 mrad horizontal and ∼175 mrad vertical acceptance (taking into account a vacuum can of 1 meter length).

B. $PbWO_4$ Detector

Projecting this to a distance of 4 meters, the front face of the $PbWO_4$ calorimeter, implies a detector of 58 cm wide and 70 cm high. This corresponds to 29 by 34 $PbWO_4$ crystals of 2.05 by 2.05 cm^2 (each 18.0 cm long). We have added one crystal on each side to properly capture showers, and thus designed our $PbWO_4$ calorimeter to consist of 31 by 36 $PbWO_4$ crystals, or 64 by 74 cm^2. This amounts to a requirement of 1116 $PbWO_4$ crystals, less than the 1152 used in the Hybrid Calorimeter of the PRIMEX experiment.

To reject very low-energy background, a thin absorber could be installed in front of the $PbWO_4$ detector. Other experiments may add a veto detector in front of the crystals, for instance consisting of 5 mm-thick segmented scintillator counters, to reject high-energy charged particles that are not deflected by the sweeper magnet. The space between the sweeper magnet and the proximity of the $PbWO_4$ detector will be enclosed within a vacuum channel (with a thin exit window, further reducing low-energy background) to minimize the decay photon conversion in air.

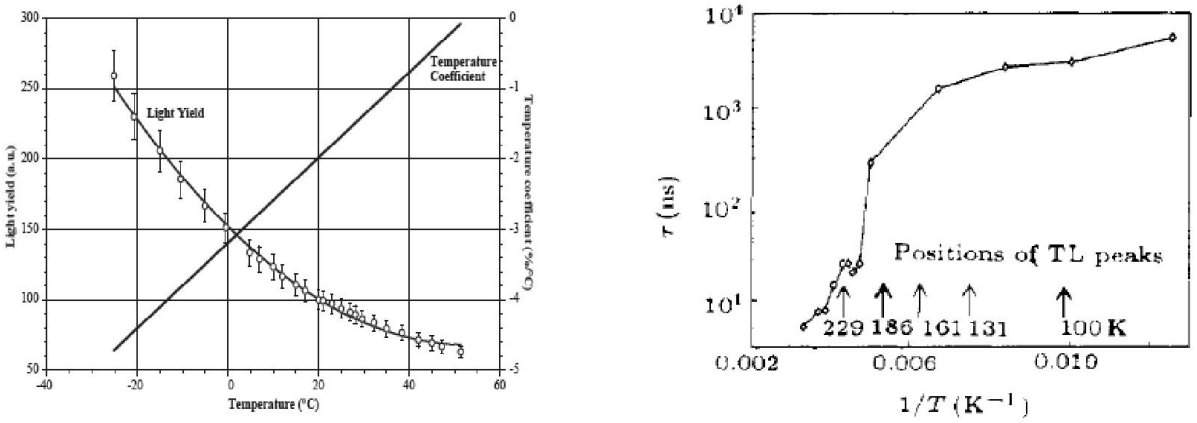

(a) (b)

FIG. 2: *Temperature dependences of the light yield (a) and the decay time of the emission of the λ=400 nm light (b) for the crystal $PbWO_4$. Figure (a) is adopted from P. Lecoq et al. [5], and (b) from Shi Chao-Shu, Chin [6].*

The emission of $PbWO_4$ includes up to three components, and decay time increases with wave length: τ_1 ∼5 ns (73%); τ_2 ∼14 ns (23%) for emission of λ in the range of 400-550 nm; τ_3 has lifetime more than 100 ns, but it counts only ∼4% of the total intensity. The light yield and the decay time of the $PbWO_4$ are temperature dependent, with the light yield increasing at low temperature (Fig. 2(a)), but the decay time (drastically) decreasing at room temperature, as illustrated shown in Fig. 2(b).

Given the temperature sensitivity of the scintillation light output of the $PbWO_4$ crystals, the entire

calorimeter must be kept at a constant temperature, to within 0.1° to guarantee 0.5% energy stability for absolute calibration and resolution. The high-voltage dividers on the PMTs may dissipate up to several hundred Watts, and this power similarly must not create temperature gradients or instabilities in the calorimeter. The π^0 calorimeter will thus be thermally isolated and be surrounded on all four sides by water cooled copper plates. This design is based on that of the HYCAL temperature controlled frame and optimized with more recent experience from CMS [7], which has shown stability to 0.05° C. The materials for the frame are foreseen to include steel and steel alloy plates, copper plates, and a temperature control system, and the design accomodates a geometrical arrangement in an array of 36 by 31 crystals.

At the anticipated background rates (see section III B), pile-up and the associated baseline shifts can adversely affect the calorimeter resolution, thereby constituting the limiting factor for the beam current. The solution is to read out a sampled signal, and perform offline shape analysis using a flash ADC (fADC) system (see section II B 2). New HV distribution bases with built-in pre-amplifiers (see section III D) will allow for operating the PMTs at lower voltage and lower anode currents, and thus protect the photocathodes or dynodes from damage.

The $PbWO_4$ detector for π° detection is located at a distance of 4 meters, and the dimensions of the $PbWO_4$ crystals are 2.05 x 2.05 cm^2. The typical position resolution is 2-3 mm. Each crystal covers 5 mrad, and the expected angular resolution is 0.5-0.75 mrad, which is comparable with the resolutions of the HMS and SOS, routinely used for Rosenbluth separations in Hall C. This can also be compared with the CLAS Inner Calorimeter (IC), which has crystals of dimensions 1.33 x 1.33 cm^2 at the front face, located at a distance of 0.8 m from the target. The CLAS IC has reached an angular resolution of 3-4 mrad [8]. Note that compared to the CLAS IC in our case the solid angle per crystal in reduced by a factor of 2.1.

The momentum resolution for exclusively-produced neutral-pions amounts to better than 1%. All these are sufficient given the anticipated less-drastic t-dependence of exclusive ^{1}H(e,e$'\pi^\circ$)p channel as compared to ^{1}H(e,e$'\pi^+$)n.

1. Geometric Acceptance of the Neutral Particle Detector

The $PbWO_4$ neutral pion detection system can in principle measure either one decay photon or two decay photons from the $N(e,e'\pi^\circ)X$ process. We consider here only events with both decay photons detected, as a means to determine the π° electroproduction cross sections. The $\pi^\circ \rightarrow \gamma\gamma$ decay is isotropic in the pion rest frame. For exclusive π° production, the electroproduced π° captures the full momentum transfer vector $\vec{q}$, and there is a strong forward boost of the decay toward the calorimeter resulting in good π° acceptance. For neutral pions following a semi-inclusive scattering process, the acceptance will become negligible at small z, where the π° momentum becomes smaller and the $\gamma\gamma$ decay angle larger, preventing coincidence γ detection. In a typical experimental configuration at a 12-GeV Jefferson Lab with a three-momentum transfer of 5.5 GeV/c, this happens at $z \sim 0.3$, where the pion energy is reduced to $E_\pi \sim 1.5$ GeV.

The geometric acceptance of the π° detector was estimated by means of a Monte Carlo calculation. The direction of the primary π° was sampled within the acceptance of the detector, with subsequent π° decay into two γ's. The fraction of events where both γ's were simultaneously detected in the calorimeter was used to calculate the geometric acceptance.

The pions originated from an assumed distance of 4 meters to the calorimeter. A Gaussian distribution of transverse momentum of the π° relative to the direction of the virtual photon was assumed. The virtual photon pointed to the center of the calorimeter, and the slope parameter of the exponential transverse momentum p_T distribution, b=4.661 $(\mathrm{GeV/c})^{-2}$, was assumed (similar to a typical b value found in charged pion production). The prompt pion decay in two photons was sampled uniformly in the π° Center-of-Mass frame, and then the γ's were boosted into the lab frame. Cases with both γ's hitting the active area of the calorimeter and energies of at least 100 MeV were scored.

An example of the geometric acceptance for the chosen detector configuration and a π° momentum in the range from 1.0 to 10 GeV/c is listed in Table I, and shown in Fig. 3. The acceptance rises with pion energy (or

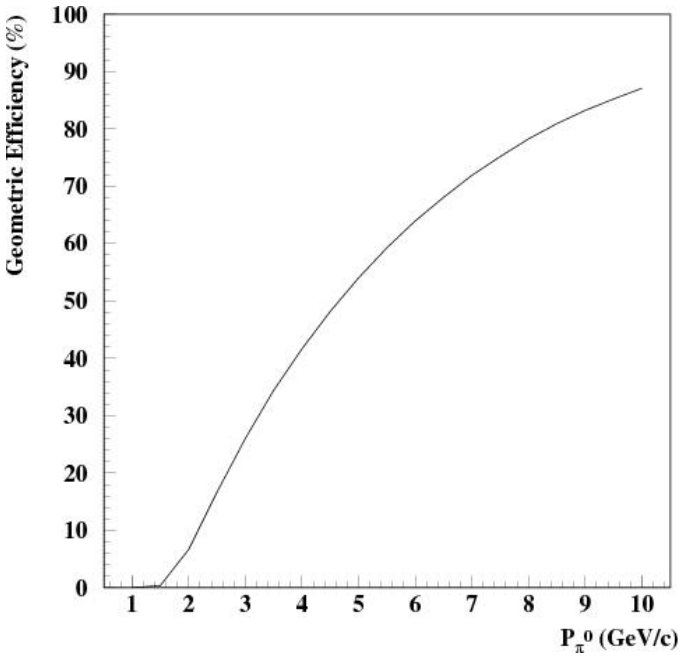

FIG. 3: The geometric acceptance of Neutral Particle Spectrometer as a function of pion momentum P_{π°.

z) due to the decrease in the $\gamma\gamma$ opening angle. Even at the highest energies, the opening angle will still be of the order of 50 mrad, providing ample separation between the two shower centroids of the decay photons, given an expected angular resolution of about 0.7 mrad (or better) for the $PBWO_4$ π° detector.

P_{π° (GeV/c)	1.0	1.5	2.0	2.5	3.0	3.5	4.0	4.5	5.0	5.5	6.0	6.5	7.0	7.5	8.0	8.5	9.0	9.5	10.0
Acceptance (%)	0.0	0.4	6.7	16.7	26.1	34.4	41.7	48.2	54.1	59.2	63.9	68.1	71.9	75.2	78.3	80.9	83.2	85.2	87.1

TABLE I: *Geometric acceptance of π° detection in a calorimeter with an 58 × 70 cm^2 active area at 4 m distance from target.*

To estimate the efficiency of selecting a photon pair from other processes at forward angles, several background simulations were performed to study the combinatoric background. The distance of the calorimeter, and relative small size of the $PbWO_4$ crystals, are beneficial for reduction of this combinatoric background. It was found that for the worst-case scenario of neutral-pion detector angle of 6 degrees, for a 1 μA beam current, a 10 cm LH2 target, and a 100 ns coincidence time window to capture the two photons, the combinatoric background is only at the few % level, as shown in Figure 4, before application of any other cuts. Thus, we feel confident that we can understand well the efficiency, and especially its stability under these assumptions. Of course, if less detailed understanding is required, one can scale and easily accept higher luminosity numbers.

To elucidate this further, in Figure 5 we present the anticipated pion detection efficiency and combinatoric background as a function of electronics threshold. This is estimated based upon realistic background simulations by P. Degtiarenko for a 10 cm liquid hydrogen target and 1 μA beam current, at the mentioned small angle of 6.3°. The background simulations will be presented in more detail later on.

2. Electronics for Neutral Particle Spectrometer

In this section we will describe the plans for the electronics for (e,e′γ), or more specific (e,e′π°) reactions. In the latter case, both photons following the decay of neutral pions will be detected in the $PbWO_4$ calorimeter, in coincidence with the scattered electron. However, for many of the anticipated kinematics pursuing moderate

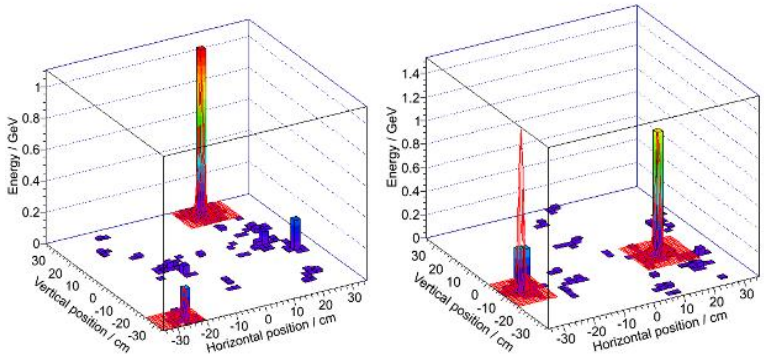

(a) *GEANT4 simulation of photons from π° decay with simulated background of neutral and charged particles, the latter suppressed by the sweeper magnet. The photon pair is selected from other processes in the calorimeter using a cluster finding algorithm.*

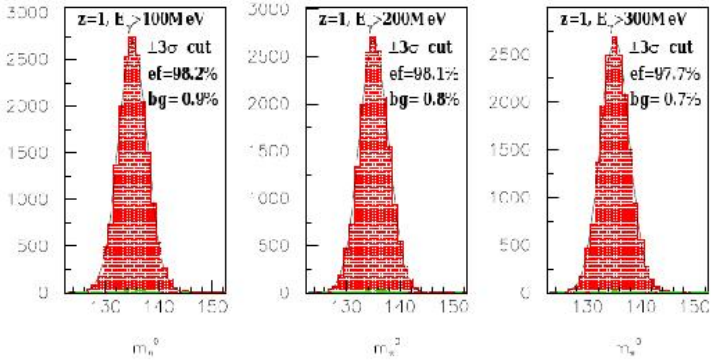

(b) *Reconstructed invariant mass of the π°.*

FIG. 4: Simulations of the $PbWO_4$ calorimeter.

to high four-momentum transfer, the singles rate of electrons in the HMS will be sufficiently low (<1 kHz) to allow using a minimum-bias electron trigger and reading out the π° calorimeter in each event. In this way, exclusive, semi-inclusive, and inclusive cross sections can be compared directly at each kinematic point.

To take full advantage of the high-resolution crystals while operating in a high-background environment, modern flash ADCs (fADCs) will be used to digitize the signal. They continuously sample the signal every 4 ns, storing the information in an internal FPGA memory. When a trigger is received, the samples in a programmable window around the threshold crossing are read out for each crystal that fired. Since the readout of the FPGA does not interfere with the digitizations, the process is essentially deadtime free. If needed, the DAQ system will support windows up to 200-300 ns at 1 kHz and 100% occupancy in the 1200 channel calorimeter ($\sim$ 200 MB/s), but projected data rates will be smaller by orders of magnitude for all presently envisioned kinematics even if the thresholds are set very low. The sampled signals can then be fitted and integrated off-line, effectively eliminating issues with pile-ups, baseline shifts, etc.

For low-Q^2 measurements, where the electron singles rate could be high, the fADC-based system can support a coincidence trigger. Such a trigger would take advantage of the ability of the fADC to perform the integration of the pulse and pass it along to the trigger for cluster finding. The appropriate conditions for the latter can then be used to select, for instance, π° or DVCS events. The integration and cluster finding will delay the trigger decision, but this can be easily accomodated in a pipelined system without any need for delay cables or analog delay modules.

In summary, the system will provide a low dead time, precision signal processing off-line, and support

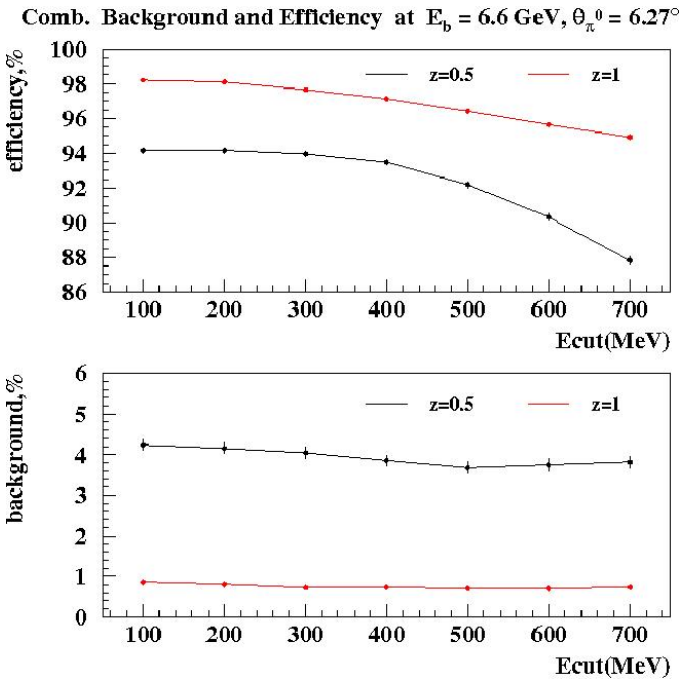

FIG. 5: The pion detection efficiency and combinatoric background as a function of energy threshold.

both high-rate operations in singles mode as well as advanced, trigger-level cluster finding in coincidence mode, As such, it will not only constitute a major advance compared with previous systems used at JLab (*e.g.*, in Hall A), but also make the most effective contribution for improvement of the existing hardware.

C. Setup and Angle Coverage

The major sources contributing to the dose are the target-induced rates themselves, and apertures of the beam line where large-thickness materials such as vacuum flanges are at the closest (critical) distance from the beam. The incident beam will scatter in the target, and (multiple) scattering products will hit such narrow sections first. Subsequently, they will locally deposit almost their full energy in the beam pipe in the form of an electro-magnetic cascade, irradiating a forward angular cone. To minimize this background, a conical or telescopic design of the initial portion of the beam exit line would be useful. This requirement routinely conflicts with the physics need to put the active detectors or spectrometers at forward angles.

Obviously, it is optimal to make the opening or critical angle for the beam exiting the target/scattering chamber region as large as possible.

For instance, if the critical angle would flare out to that determined by the two-feet diameter last section of the beam exit line far downstream, about a degree, then the main cone of scattered electrons would remain inside the vacuum pipe until well beyond the envisioned active detector and its background. This way, the general background in the Hall will be significantly decreased, typically by a few 10's of % at higher beam energies, although much larger at lower beam energies.

The present "standard" critical angle for the Hall C configuration allowing for the smallest spectrometer angles (the so-called "small-angle beam pipe assembly") amounts to an 8.6 mr critical angle, induced by a two-inch diameter beam pipe up to a distance (from the pivot) of 2.96 m. The so-called "large-angle beam pipe" has a two-inch diameter beam pipe to only 1.45 m instead, and thus reaches a critical angle of 17.5 mr, nearly matched to the optimal flare of 1 degrees. However, the HMS can only reach a 15 degree scattering angle with this "large-angle beam pipe" assembly. The reason is that the HMS-Q1 (at a distance of a bit beyond 1.5 m) has a slot on the beam axis side, with a vertical dimension of 2.9 inches.

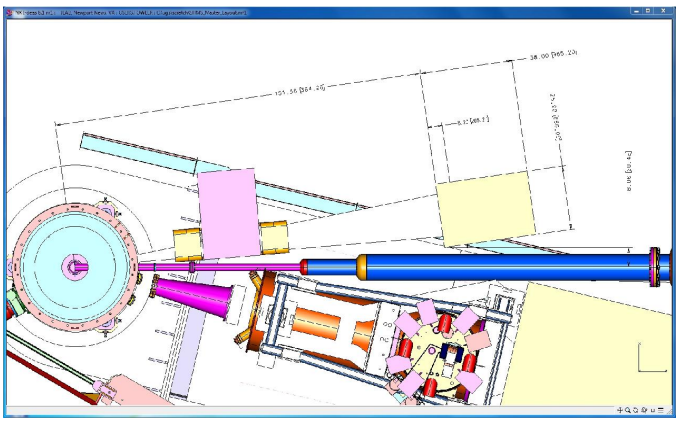

FIG. 6: *Modified beam pipe assembly for the beam dump line. The initial beam pipe has a 2.5 inch diameter up to a distance of 2.35 m, just beyond the area where HMS-Q1 has a slot. Then, the beam pipe has a short section with 6 inch diameter, followed by a long 12-inch diameter section. With this beam pipe, the critical angle will be 13.5 mr. The HMS can rotate to 10.5 degrees (albeit only locally below 13 degrees), and NPS can reach its foreseen smallest angles.*

Hence, we plan to design a beam pipe with 2.5 inch diameter up to a distance of 2.35 m (beyond the slot in HMS-Q1), then flaring out to a larger diameter. This modified beam pipe assembly is illustrated in Fig. 6. It allows HMS to achieve its smallest scattering angle of 10.5°, albeit at the cost of sacrificing remote rotation for HMS below 13° or so, as the beam pipe fits snug into the HMS-Q1 slot. The modified beam pipe assembly does allow the NPS to reach its design smallest angle of 5.5° (equivalent to the smallest angle reach of SHMS) for a distance to the $PbWO_4$ calorimeter of 4 m. With this modified beam pipe assembly, we will achieve a critical angle of 13.5 mr. Note that this is the critical angle corresponding to the background simulations presented later. The general background for beam energies of 6 GeV and higher is for this beam pipe assembly dominated (90%) by the background generated directly in the beam-target interactions. Additional shielding can be considered between the beam line and the $PbWO_4$ calorimeter, near the critical distance.

For the envisioned wide-angle Compton scattering experiments, the typical angle of the NPS is much larger. For these experiments, especially as they plan to use both an 8% Cu radiator and a target, the induced bcakground in the beam line may provide a larger contributions inducing the need for additional lead shielding between the beam line and the detector. In that sense, it can be much more efficient to use a second beam pipe with increased flare or critical angle - for experiments that do not drive the smallest HMS or NPS angles we could have a beam pipe assembly with flare close to the optimal critical angle of a little beyond one degrees.

In fact, such wide-angle Compton scattering experiments drive the need for an NPS at large angles. This can be achieved by installing the NPS directly on the SHMS platform under the secondary platform for the magnet power supplies, on the right hand side (looking upstream) of the SHMS Quadrupole Magnets. In this configuration, the HB magnet still needs to be removed to make space for a sweeping magnet, and one of the stands for the magnet power supply platform needs to be removed. This is possible with the implemented design for this SHMS platform.

In Fig. 7 the proposed setup for an experiment in Hall C requiring photon or neutral-pion detection at large angles, such as wide-angle Compton scattering, is shown. With this setup, angles of up to 60° can be achieved.

D. Electron Identification and DAQ

In foreseen (e,e′π°) proposals [9], we will typically be detecting electrons with momenta ranging from ∼1.5 GeV/c to about 6 GeV/c in the HMS. The HMS has a lead-glass calorimeter and a heavy-gas atmospheric Čerenkov detector for electron identification. Singles rates are typically constrained in HMS to a level of 0.5 MHz

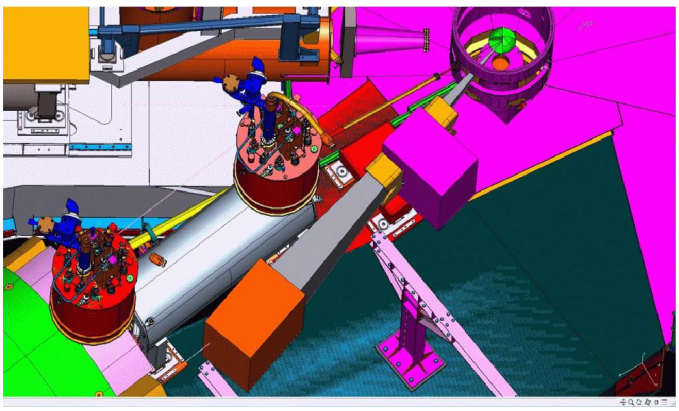

FIG. 7: *Proposed setup for a wide-angle Compton scattering (WACS) experiment in Hall C. Starting with the cylindrical scattering chamber, a sweeper magnets can be seen, followed by a vacuum channel or Helium bag, and the $PbWO_4$ calorimeter in its temperature-controlled frame. The secondary platform that holds the magnet power supplies has been removed for visualization, but the stands and supports of the secondary platform can still be seen. With this configuration, an angle range betwen $\sim 20^\circ$ and 60° is foreseen.*

to allow for a detailed understanding of the tracking efficiency. This is not an issue for the present experiment, where HMS singles rates are expected to be less than 2 kHz (see the E12-06-104 proposal [10] for detailed single rates and π/e ratios).

A good pion/electron separation has routinely been achieved in the HMS. The current detector stack of the HMS has been shown to easily achieve e^-/π^- to $\sim 10^3$, with 98% efficiency for electron detection.

In proposal [9], the π/e ratio is never larger than 130:1. Because of the moderate pion to electron ratios, we require the events of interest to only pass some loose particle identification before generating an HMS trigger. In order to have a high efficiency for electrons, a trigger will be accepted as a true electron if either the gas Čerenkov detector has fired or if the electromagnetic calorimeter has had a large enough signal.

This will allow high electron efficiency even if one of the two detectors will have a low efficiency.

The electron trigger (ELREAL) will thus have two components: Electron High (ELHI) and Electron Low (ELLO). ELHI will require a high calorimeter signal, but no gas Čerenkov detector information, and will be composed of a high signal in the "preshower" (PRHI) and a low signal in the full calorimeter (SHLO), in coincidence with scintillator signal (SCIN).

Note that the "preshower" for the HMS is simply the first layer of the calorimeter. ELLO will require a gas Čerenkov detector signal. The final HMS trigger (COIN) will be a combination of electron (ELREAL) and sampled pion (PION) triggers, the latter requiring a standard three-out-of-four (3/4) coincidence of the x-y hodoscopes (SCIN), vetoed by a gas Čerenkov detector signal (CER).

The DAQ will record both coincidence triggers between the HMS and the neutral-pion arm, as well as single-arm HMS triggers with inclusive (e,e$'$) and (e,h) events. The latter will not require readout of the pion calorimeter, and the rate can be pre-scaled if necessary. However, given the low inclusive (e,e$'$) rates at a 1 μA beam current, we plan to include all these events in the data stream. This is important for two reasons: i) SIDIS pion multiplicities can be directly formed by taking a ratio of coincidence (e,e$'\pi^\circ$) yields and inclusive (e,e$'$) yields; and ii) the inclusive (e,e$'$) yields will provide an additional normalization for the coincidence data.

In the off-line analysis, one can further use a cut on the coincidence timing between the scattered electron and the π°. Regular cuts on kinematic variables, such as the vertex position, the HMS collimator image, etc., can also be used to reduce any background, although likely not always needed, as requirements of the foreseen π°-detection experiments [9] are modest. For exclusive π° production, an appropriate cut on missing mass will be included to guarantee exclusivity of the p(e,e$'\pi^\circ$)p events.

III. BACKGROUNDS AND RADIATION DOSES

A. Overview

To preserve a high and constant neutral-pion trigger efficiency during the experiment, special attention must be paid to the calorimeter radiation damage in order to avoid problems when using a high threshold in the trigger electronics. Radiation damage is determined by both instantaneous dose rate and integrated dose. The radiation dose absorbed by the calorimeter blocks at angles less than 10° is dominated by Moeller electrons.

For the $PbWO_4$ crystals such radiation effects have been tested in HEPI (Protvino, Russia), at Brookhaven National Laboratory, and at CERN. At low dose rates (15-20 krad/h or less), and at integrated doses below 10 krad only a 2-3% degradation effect of $PbWO_4$ was observed [11].

The radiation damage dramatically increases at higher doses. For example, at a dose rate of 100 krad/h the radiation damage amounts to roughly 5% degradation, while the crystal degradation reaches 10-25% [11, 12] at a dose rate of ∼500 krad/h and integrated dose of 1-2 Mrad.

Without exceptions, in all cases the loss of resolution is attributed to degradation of the transmission properties of the blocks, and not to the degradation of the photocathode of the PMTs.

The simulated total dose rates amount to 274 rem/h when averaged over an angle of 5-25 degrees, and calculated for a 1 μA beam current, a 10 cm long cryogenic hydrogen target, and a beam energy of 6.6 GeV. We have verified that the background rates only slightly depend on the beam energy, with simulations at 6.6 and 11 GeV agreeing at a better than 20% level. A 7.5 kG sweep magnetic field reduces these dose rates to 18 rem/h. The dose rates fall rapidly as the angle increases from 5 to 25 degrees, by approximately one order of magnitude, and are, as expected, dominated by (Moeller) electrons. At 5.5 degrees, the dose rates correspond to 400 rem/h (without field) and 50 rem/h (with field), respectively.

Given that we anticipate only limited kinematics close to this smallest angle of 5.5°, with more typical kinematics at ∼8° and beyond, the dose rates look modest and certainly easily acceptable for a 1 μA beam current assumption and the proposed sweeping magnet. In addition, we have prepared and tested custom pre-amplifiers in order to operate the PMTs at lower high voltages, with lower anode currents.

More details on the rate simulations and the modified voltage divider design can be found in sections III B and III D. We come back in details to the anticipated radiation dose effects and allowable radiation doses by the improved setup in sections III E and III F.

B. Electromagnetic Background Simulations

We will use $PbWO_4$ blocks similar to the inner high-resolution part of the Hybrid Electromagnetic Calorimeter (HYCAL) [4] for the detection of the photon-pairs from π° decay. The HYCAL calorimeter has previously been successfully used in JLab's Hall B PRIMEX and PRIMEX-II experiments, to precisely measure the neutral pion's lifetime. Energy and coordinate resolutions of $\sigma/E = 1.3\%$ and σ_x ∼1.28-2.10 mm have been achieved at a neutral-pion energy of 5 GeV.

For the envisioned small angles the neutral-pion detector will operate at high rates, and associated high radiation dose. In such conditions, the $PbWO_4$ crystals can accumulate doses that would damage their transmission properties. This would result in a loss of energy resolution of the calorimeter, which in turn worsens the missing mass resolution. Special attention must be paid to the detector background condition.

The background rates and the NPS radiation doses (for now without the effect of the sweeping magnet included) have been calculated by Pavel Degtiarenko [13]. The various particle rates as a function of angle and particle energy as induced by the interaction of a 6.6 GeV electron beam and a 10 cm liquid hydrogen target are shown in Figs. 8 and 9, for photons, positrons, electrons and positively-charged pions, as examples. These rates are for a 1 μA beam current and a 10 msr solid angle detector.

Given the strong angular dependence of background rates, we only show the rates and radiation doses for angles smaller than 20° in Figs. 8 and 9. Rates at larger angles are completely negligible compared to this.

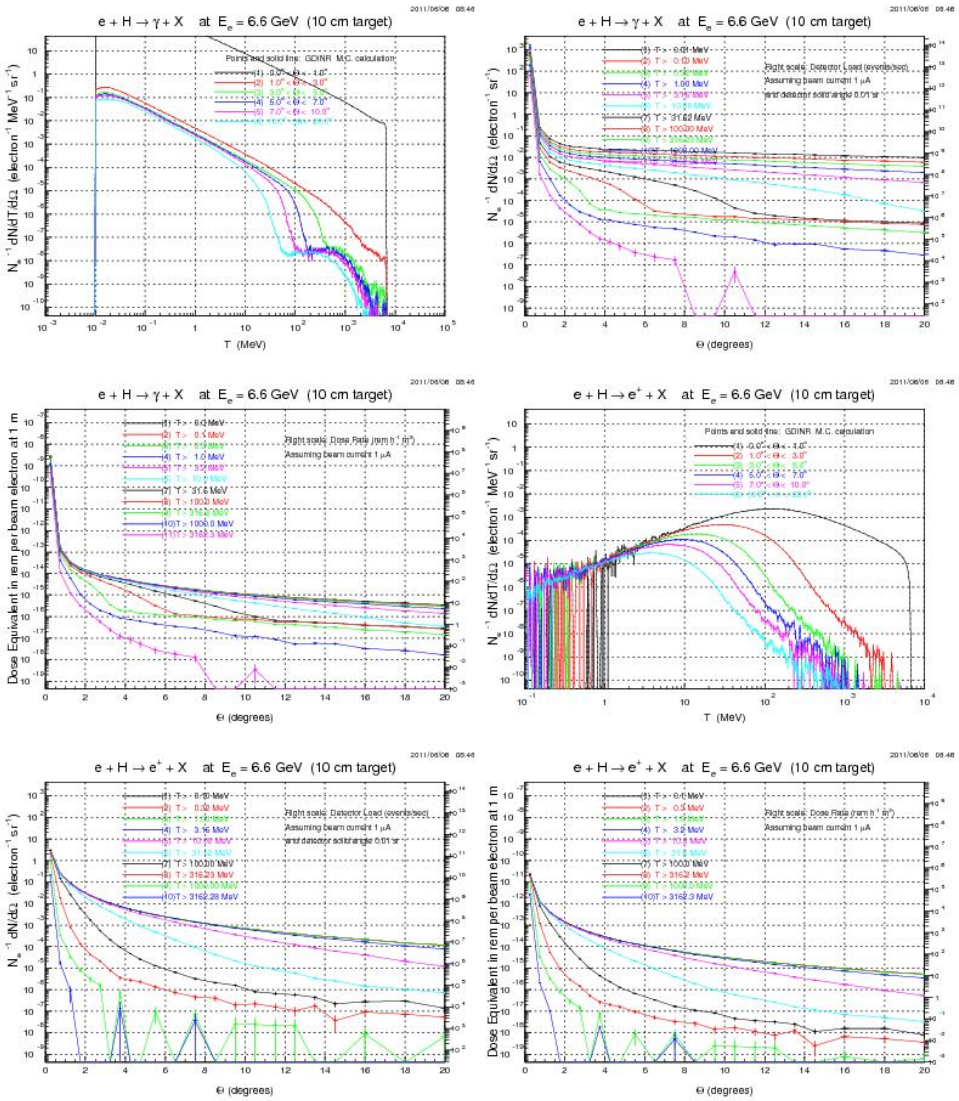

FIG. 8: Expected particle background rates and the radiation dose as seen by a 10 msr detector for photons and positrons, assuming a beam energy of 6.6 GeV, a beam current of 1 μA, and a 10 cm LH2 target.

This strong angular dependence is further highlighted in Table II, which shows the estimated rates (events per second) for photons, electrons and positrons for a detector with solid angle of 10 msr positioned at 3.5, 6.0 and 8.5 degrees, respectively.

Taking into account that we plan to use a ∼1000-channel lead-tungsten calorimeter with a solid angle of about 25 msr, the particle rates will be higher by factor of 2.5, resulting in a rate per crystal of over 2 MHz for angles $\leq$6 degrees, with the major fraction of the rates produced by Moeller electrons. It is obvious that the use of a magnet to sweep these electrons is essential.

Fig. 10 shows the layout as used in the simulations. It includes the 10 cm LH2 target located inside the 12-GeV-compatible existing Hall C scattering chamber. The mechanical dimensions of the HB magnet with its bore are used to indicate the yoke and position of the sweeping magnet, bending electrons inwards (towards smaller angles). Here, a 7.5 kG magnetic field is simulated, corresponding to 0.3 Tm. The front face of the detector is at a distance of 4 meter from the target, and covers in this layout an angular range between 5 and 25 degrees. The black dashed-dotted lines correspond to angles of 3, 5, 15, 25 and 28 degrees, respectively. The red

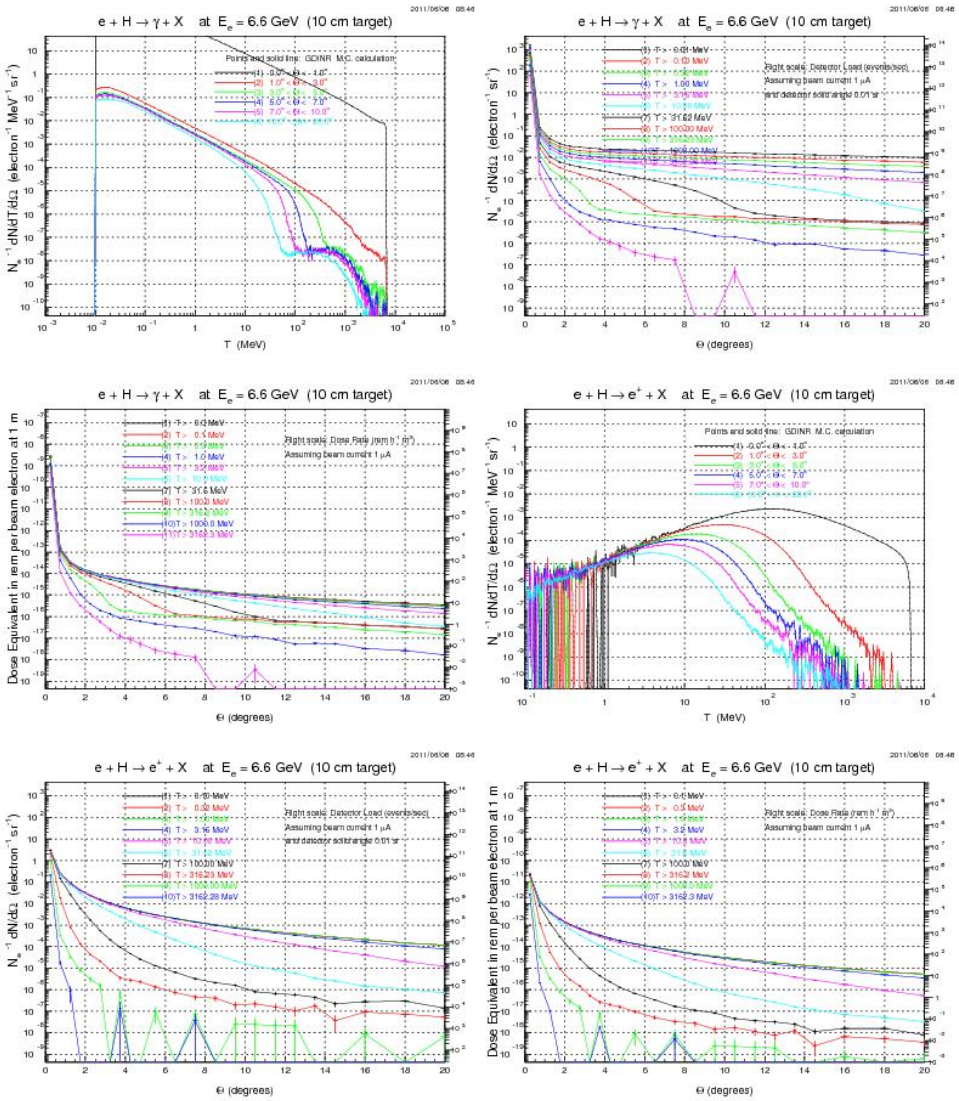

FIG. 9: Expected particle background rates and the radiation dose as seen by a 10 msr detector for positrons and π^+, assuming a beam energy of 6.6 GeV, a beam current of 1 μA, and a 10 cm LH2 target.

track shows the trajectory of a 500 MeV electron emitted at an angle of 15 degrees. We note that the 0.2-0.3 Tm design requirement of the sweeping magnet is driven by guaranteeing sufficient bending power to sweep away up to 300 MeV electrons. This has a tremendous impact on the particle rates shown earlier in Fig. 9 (top right panel).

Figs. 11(a) and 11(b) further show simulated trajectories for 10000 beam-electrons with an energy 6.6 GeV, with the sweep magnetic field "OFF" and "ON", respectively. Blue and red tracks correspond to photons and charged particles, respectively, and the "cleaning" effect of the sweeping magnet can be readily seen.

To quantify the effects of the sweeping magnet further, the results of the dose rate calculations (in rem/hr) for a 1μA beam current and a 6.6 GeV beam energy, with a 7.5 kG magnetic field (0.3 Tm) OFF and ON are presented in Table III. We note that the presented results are *averaged* over the 5-25° detector front face. The dose rates fall rapidly as the angle increases from 5 to 25 degrees, by approximately one order of magnitude. At 5.5 degrees the dose rates correspond to ∼400 rem/hr for the field OFF, and ∼50 rem/hr for the field ON

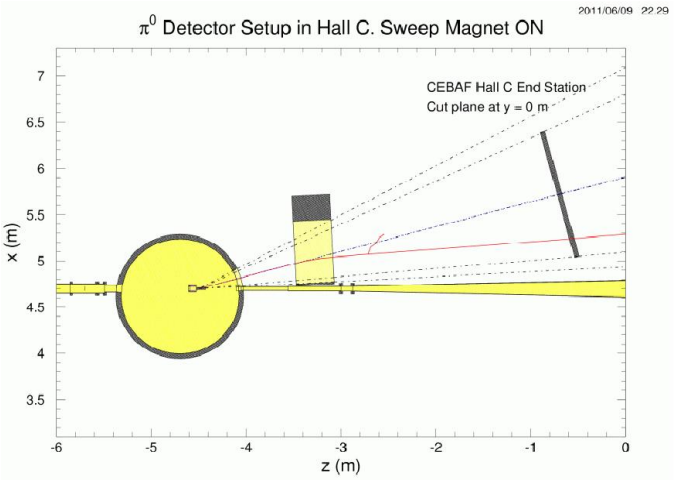

FIG. 10: The schematic layout of the sweep magnet.

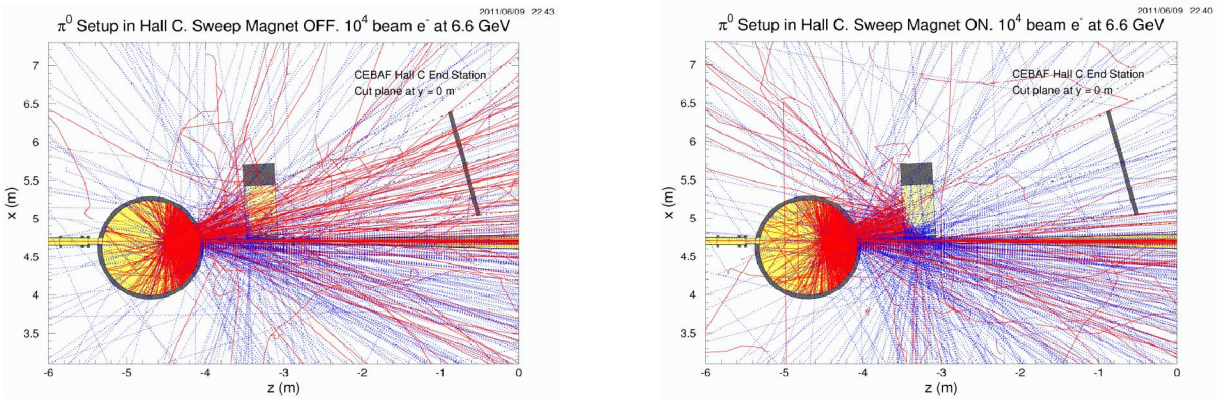

(a) (b)

FIG. 11: *(a): Simulated trajectories for 10000 beam electrons with an energy of 6.6 GeV, with the sweeping magnet OFF.(a) and ON (b) configuration*

configuration. The latter looks certainly acceptable.

We further illustrate the results of detector count rates as simulated with the well-calibrated GEANT3 code used for successful execution of all JLab experiments in Fig. 12. The six panels correspond to three different energy thresholds each, with the sweeping magnet both ON (left panels) and OFF (right panels). The flux is in the Hz/cm^2 units, at the front face of the neutral particle detector and is a function of the position horizontally along the detector, and away from the beam line. The bin sizes correspond roughly to steps of one degree in the scattering angle.

Particle	3.5°	6.0°	8.5°
Electron	3×10^9	6×10^8	6×10^6
Positron	6×10^6	6×10^5	2×10^5
Photon	4×10^8	2×10^8	1×10^8
Total	3.4×10^9	8×10^8	1×10^8

TABLE II: Particle rate (event/sec) for a detector with solid angle of 10 msr located at an angle of 3.5, 6.0 and 8.5 degrees, respectively. These rates assume a beam energy of 6.6 GeV, a beam current of 1 μA, a 10 cm long LH2 target, and no sweeping magnet.

	Magnet OFF	Magnet ON
Photon dose rate	3.03±0.03	2.81±0.03
Positron dose rate	5.43±0.13	3.75±0.11
Electron dose rate	265.23±0.95	11.48±0.23
Total dose rate	273.69±0.96	18.04±0.26

TABLE III: Simulated dose rate (rem/hr) for a 1 μA beam current and a 6.6 GeV beam energy, with a 7.5 kG (0.3 Tm) magnetic field OFF and ON. The errors are purely statistical and somewhat underestimated as a Gaussian approximation has been used for a distribution that is significantly non-Gaussian.

With the magnetic field added, the dominant source of the background rates now become photons with an energy above 10 MeV and electrons with an energy above 100 MeV. As one would have anticipated, the use of a relatively simple sweeping magnet will dramatically reduce the (Moeller) electron rates. At the smallest angles foreseen, the rate of photons with energies $E_\gamma > 10$ MeV is $N_\gamma \sim 3 \times 10^5$ Hz/cm^2. For $PbWO_4$ crystals with dimension of 2.05×2.05 cm^2, the photon rate per crystal is $\sim 1.2 \times 10^6$ Hz. The electron rates with energy E_e >100 MeV is $N_e \sim 6{\times}10^5$ Hz/cm^2, or $\sim 2.5{\times}10^6$ Hz/crystal without sweeping field, and drops to $N_e \sim 5{\times}10^4$ Hz/cm^2, or $N_e \sim 2 \times 10^5$ with sweeping field. This shows the sweeping magnet has, as designed, also still quite some impact on electrons with energy above 100 MeV.

In Fig. 13(a) and Fig. 13(b) we show the flux of photons, electrons and positrons as determined from the detailed numerical results underlying the expeeted background rates in Figs. 8 and 9, for a photon threshold energy of 10 MeV and an electron (or positron) threshold energy of 100 MeV. The $PbWO_4$ detector is asumed to be at a 4 meter distance from the target, and cover a solid angle of 10 msr. Note that this is smaller than the envisioned $PbWO_4$ detector, but this will be taken into account later. Each $PbWO_4$ crystal has a 2.05 by 2.05 cm^2 size, and covers a solid angle of 0.025 msr. The 10 msr case corresponds to the top panels of Fig. 13(a) and 13(b), the single $PbWO_4$ crystal case corresponds to the bottom panels. The flux is shown for two cases, without and with a sweeper magnet (Sweep OFF and ON), in Figs. 13(a) and 13(b), respectively.

In Fig. 14 we illustrate the photon flux, for the sweeper magnet on situation, but as a function of the photon energy threshold ranging from 1 to 100 MeV. As anticipated, the flux drops with angle increase. For higher thresholds, the drop can be initially very fast at smaller angles, and more graduall at larger angles. This is due to the drop of the electron flux generating the photons. For instance, the photon flux can drop by a factor of ∼100 for the energy range from 0.5 to 200 MeV, thus higher thresholds will give drastically reduced fluxes.

The major sources of the background were found to be the target-induced rates, with the induced background from beam line componets contributing perhaps 10-20%. We did verify that the background conditions for an 11 GeV beam energy are nearly similar to a 6.6 GeV beam energy, through are overall some 10% smaller for all angles. Thus, all the background rates given for the 6.6 GeV beam energy give a very good representation of an 11 GeV beam energy too.

C. Detector Linearity and Efficiency

Studies have shown that detector performance (particularly the PMT gain) may change by few-percent to few-tens-of-percent level for a high flux (at dose rates > 1 Rad/hr). The scale of this change of performance depends on the type of crystal, the PMT and on other components of the hardware.

Two types of $PbWO_4$ crystals, SIC and BTCP, have shown opposite behavior in the detector response above dose rates equivalent to 4 GeV electrons at ∼ 50 kHz in an early low-current electron beam test of the PRIMEX collaboration [14]. This behavior could be caused by three effects:

- change of the scintillation mechanism in the crystals;
- change of the light transmission in the crystals;
- change of the PMT gain due to rate variations.

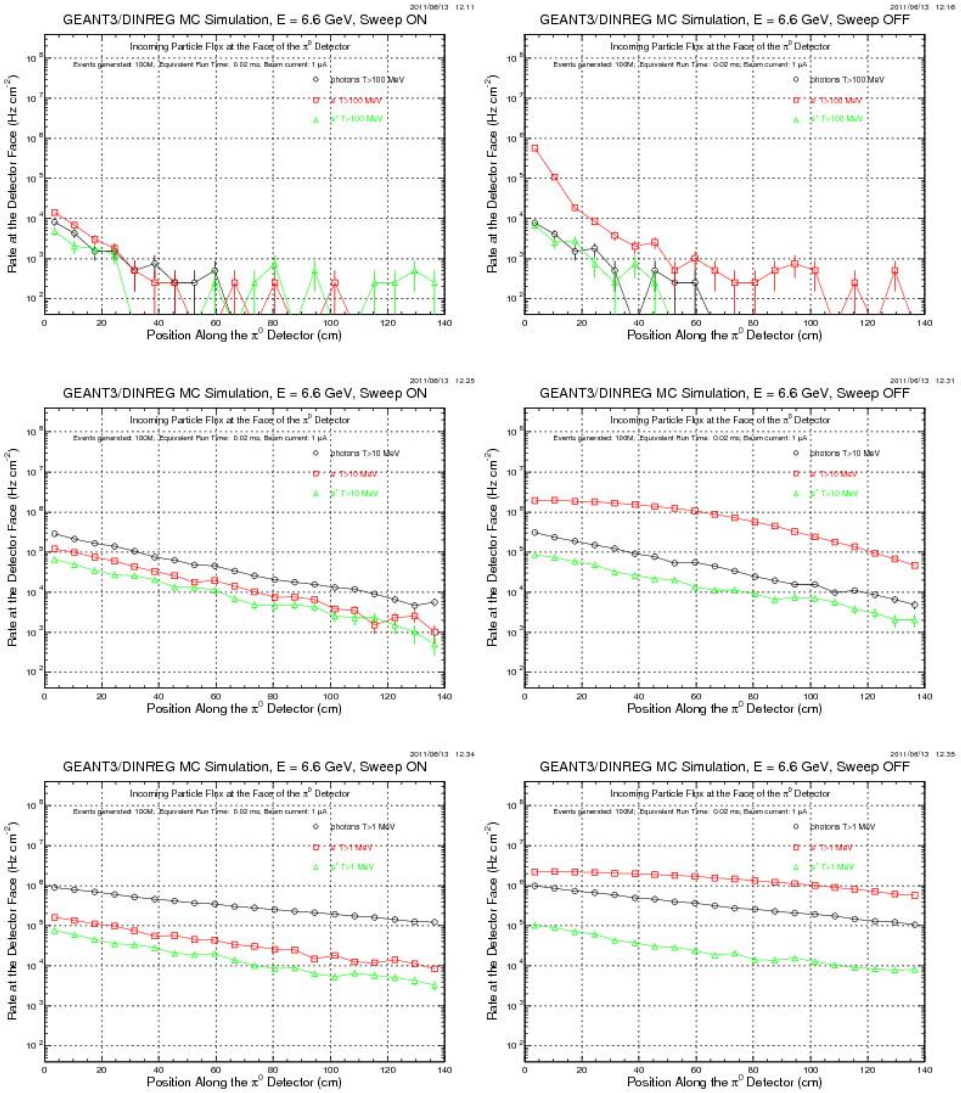

FIG. 12: Simulated flux of the particles (in Hz/cm^2) at the face of the detector as a function of the position (in cm), at three energy thresholds (from top to bottom 100, 10 and 1 MeV) and with the sweeping magnet ON (left) and OFF (right).

The results of the PRIMEX studies of the PMT gain variation with rate are presented in Fig. 15.

The overall variation of the measured signals relative to their values at modest rates (for 4 GeV electrons) was found to be small, $\pm 1\%$, up to rates of about 10^5 Hz. Beyond such high rate, deviations grow fast, which is understandable as such a high rate will require a PMT with a fast response, operated at low gain and low anode current. The construction and use of custom pre-amplifiers to allow operation of the PMTs at lower high voltages, and to compensate the gain reduction, will offer a solution for high rates. We will describe such modification and subsequent performance tests later.

The loss of amplitude is considered to be due to degradation of the transmission properties of the blocks, but not because of degradation of the photo-cathode of the PMTs. Hence it is possible to cure any radiation damage by exposing the $PbWO_4$ crystals to near-UV blue light. A continuous monitoring of the crystal performance through physics measurements (like elastic $e-p$ scattering, or π° mass reconstruction) can be considered, if possible, and, pending on the experimental situation curing cycles can be integrated. We estimate such a curing

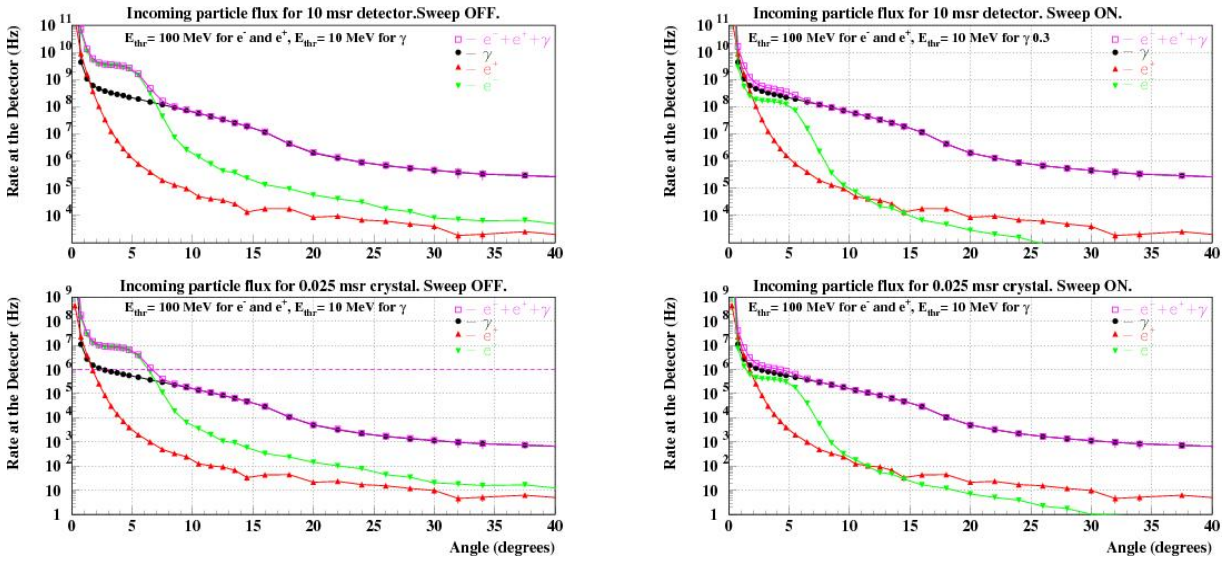

(a) (b)

FIG. 13: *The flux of the particles for the 10 msr detector and 0.025 msr single crystal as a function of the angle at energy thresholds 10 MeV for photons and 100 MeV for electrons and positrons. The detector (crystal) is at the distance of 4 m from the 10 cm LH2 target. The beam energy and current are 6.6 GeV and 1.0 μA. The sweep magnet is OFF (a) and ON (b).*

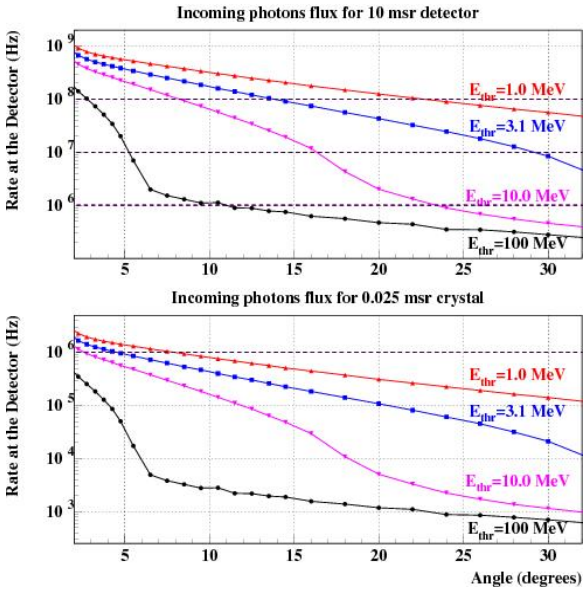

FIG. 14: *The flux of the photons of the 10 msr detector and 0.025 msr single crystal as a function of the angle at energy thresholds 1.0, 3.1, 10 and 100 MeV. The detector (crystal) is at the distance of 4 m from the 10 cm LH2 target. The beam energy and current are 6.6 GeV and 1.0 μA.*

cycle to require in general a shift. It may well be possible to do such a curing cycle during an opportunistic beam studies or beam down times.

As is described in more detail in section III B, the main source of background in the detector is low-energy photons. In the worst-case scenario (central angle of about 5.5°), the background rate is expected to be 200 MHz within the calorimeter acceptance, or on average 200 kHz per module. These rates are under the assumptions of 1 μA beam current impinging on a 10 cm LH2 target, with high (6-11) GeV beam energies and with the

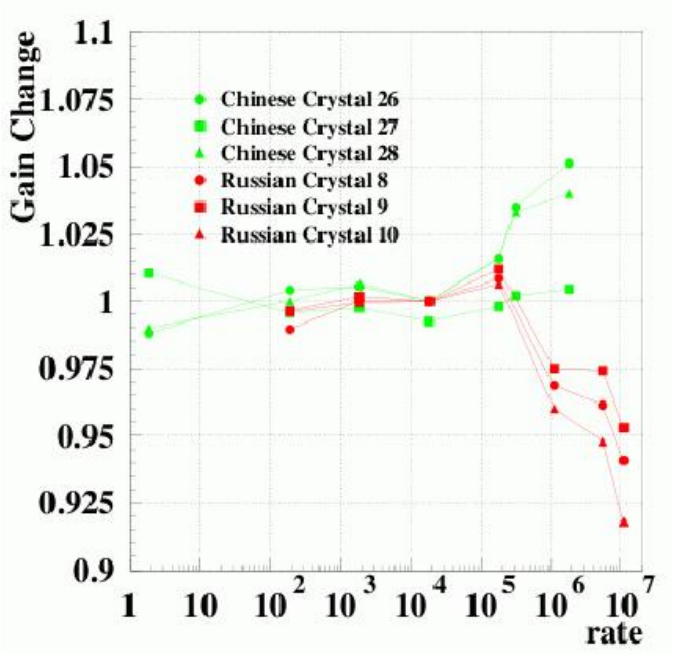

FIG. 15: The variation of the PMT gain for two different types of $PbWO_4$ crystals as tested for the PRIMEX apparatus, as a function of the rate induced in a low-current electron beam test. (Adopted from [14]).

$PbWO_4$ detector at a distance of 4 meters. Of course, the rate of the background is not uniform, and will in this worst-case scenario be a factor of 2-4 higher for the crystals closest to the beam line, at about 3.5°. The dominant fraction of these photons has energies below 10 MeV, which is in order of the critical energy of 8.5 MeV, where ionization and Cherenkov radiation losses are equal. But, these low-energy photons can still cause pile-up and additional anode current.

The latter is not a real issue, as shown in Fig. 16, which shows that the PMT gain variations can be controlled to better than 1% at up to 1 MHz rates per crystal if one abandons the PMT base design of the PRIMEX experiment and rather adopts a modified PMT base design [15]. The new modified active base design gives a factor of ∼25 improvement in gain stability over the existing PRIMEX bases. The tests and base modifications are described in detail in Section III D.

Given that we ultimately expect linear gain over the anticipated rates of the $PbWO_4$ crystals, the photon background will act solely as an energy baseline shift. We will use the exclusive ^{1}H(e,e′π°)p reaction here as an example to show the impact on expected detector stability and hence systematic uncertainties. First recall that in such an experiment we can overdetermine neutral pions both from the measured energy and the decay angle. Second, if we can reduce the background rates, the baseline shift will become less important and will be actually small even within a 100 ns gate. Assuming an average photon energy of 10 MeV, the rates mentioned above, and a few crystals firing for each decay photon shower, we would get a baseline shift of less than 10 MeV in a 100 ns gate. This is well within the expected energy resolution of the $PbWO_4$ crystals for photons associated with some 2-5.5 GeV (or higher energy) neutral pions.

Details on the performed rate simulations were already given in section III B. Given an average background rate of well below 1 MHz per crystal, and maximum rate of 1 MHz in the crystal closest to the beam line for a neutral-pion setup at a worst-case minimum angle of 5.5°, we conclude that the gain is stable to about 0.2% for all anticipated kinematics and background conditions (assuming here again a 1 μA beam current impinging on a 10 cm LH2 target). One can scale to different conditions.

As in the PRIMEX experiment, we have included a temperature-stabilization system in the design, hence contributions to gain stability due to temperature dependences are small, <0.2% (a 0.1°C temperature stability guarantees a 0.5% energy stability for absolute calibration and resolution).

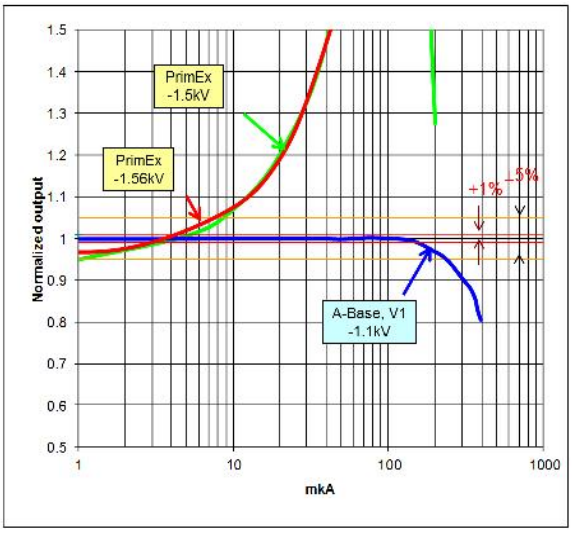

FIG. 16: *The PMT gain stability as a function of anode current. The thin solid red horizontal lines denote stability to 1% and the yellow solid lines stability to 5%. The new active base design A-Base [15], V1 outperforms the PRIMEX bases by a factor of about 25.*

Earlier we have shown the combinatoric background to be also small, <1%. We likely will know this background to a fraction of %. Nonetheless, since the background conditions change with angle, we conservatively assign an uncertainty of about 0.2-0.5%.

Lastly, the uncertainty in the geometric acceptance is correlated with the knowledge of survey and actual beam position, but will be well known (<0.1%). Overall, we feel we can achievably assume the the detection efficiency for this example of π° experiment to be stable to <0.5%.

D. Test Results for R4125 Photomultiplier Tubes with Active Bases

To increase the gain stability at the high rates anticipated with the NPS setup we have redesigned the R4125 photomultiplier used for the $PbWO_4$ crystal readout during the PrimEx experiment to have an active base. Here, the amplifier was powered from a high-voltage division chain. An initial "V0" base was tested by using a 5 mm^3 cube of Pr:LuAG scintillator to simulate a light pulse wave form similar to that of a $PbWO_4$ crystal, albeit with a factor of 200 more light output. This setup allows to simulate light corresponding to a few hundred of MeV energy deposited in $PbWO_4$ using common gamma sources. The setup was equipped with an LED diode to map the gain dependence as function of anode current. Results were encouraging, and a large gain factor ($\sim$ 25) was established with respect to the Primex existing base.

Nonetheless, these test results of the first prototype still showed a problem similar to the behavior of the original PRIMEX base, in that both base circuits use a simple passive division and are sensitive to the anode current. The tube gain then varies as function of anode current (or equivalently count rate), which could introduce a rate-dependent gain modulation. This effect is related to the current drain from the last dynodes of the division chain. It was compensated by equipping the base with two transistors connected to the last dynodes, and stabilizing the voltage on dynodes 9 and 10. The divider drain current and division ratio remained unchanged. Fig 17 shows the modified High Voltage division chain, termed the "V1" base.

The count rate capability of the modified base circuit was tested with a double LED setup.One of these LEDs was powered from pulse generator, whereas the second LED was connected to a regulated DC current source. The LED light pulse shape was tuned to ~18 ns FWHM, mimicking a scintillator pulse shape and similar to the pulse shape of the original PrimEx base (see Fig. 18(a)). In Fig 18(b) we show the High Voltage base design which was used in the PrimEx experiment (top) and the modified active base (bottom).

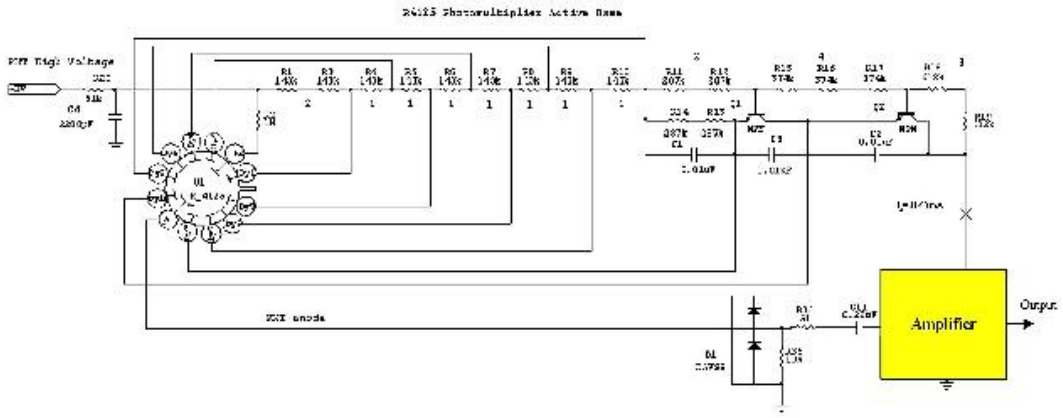

FIG. 17: *R4125 Photomultiplier tube active base circuit diagram. Two (Q1, Q2) high voltage transistors are added to the last two dynode (9 & 10) power connection nodes.*

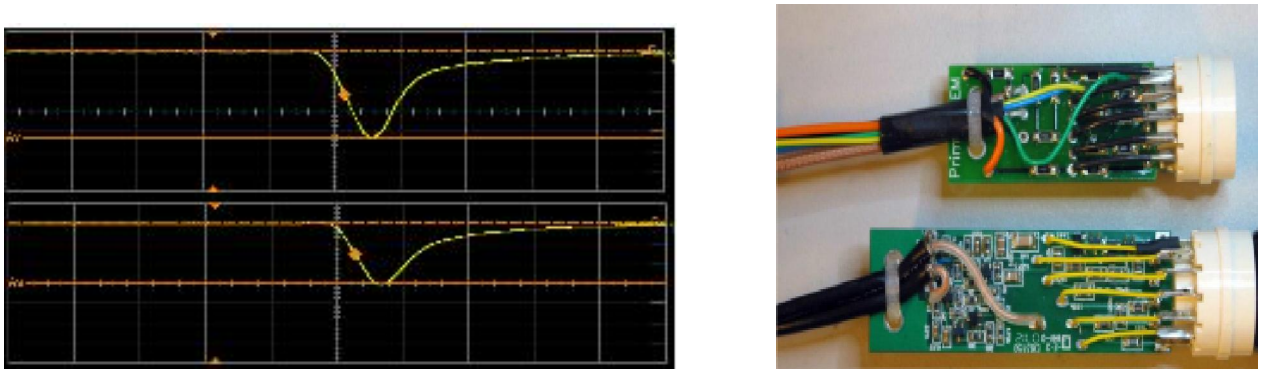

(a) (b)

FIG. 18: *(a) LED pulse waveforms recorded from the original PrimEx (top image) and the redesigned active base (bottom image). The horizontal scale is 20 ns per division, the vertical scale is 100 mV per division, for both images. Both records are acquired at 10 kHz LED pulse frequency. (b) Design of passive base (top) used in the PrimEx and the new active base (bottom) developed by V. Popov [15].*

The high-voltage bias was -1.1 kV for the new active base, where it was -1.56 kV for the original PrimEx base, to maintain about 300 mV output pulse amplitude for both PMT bases. The passive base output current is not different from the anode current, while the active base effective output current is about 10 times higher. Fig. 16 presents the summary of our tests. The results obtained from testing of our first version "V0" base (without transistors in the division chain) are included. Note that we find the gain function as function of anode current for the PrimEx bases to be consistent with either technique: using a scintillator with gamma source and measuring the photo peak, or using the LEDs either by pulsing of DC power source.

The active base design can be seen to have improved gain stability with an efficient output signal range up to $\sim 160\ \mu$A. In this range, the PMT base system gain, or pulse amplitude and pulse width, remain stable to within 1%. The measured pulse rate at this current corresponds to a rate of about 1.2 MHz of 300 mV output pulses. The PrimEx base during the test with the same LED light pulses on the other hand has a noticeable strong PMT-and-base system gain dependence as function of count rate (or anode current). With the same LED light setting, the original PrimEx PMT/base is running out of a $\pm 5\%$ gain stability range at a count rate of $\sim$ 30 kHz. The maximum anode current for linear operation of the active base has not changed, being proportional to the divider drain current which remains the same. Table IV summarizes the comparison between the various PMT bases.

In summary, the total count rate advantage of the newly designed active base remains unchanged between

TABLE IV: *Comparison of the original PrimEx base (and accompanying PMT) with the modified "V1" active-base design.*

Parameter	PrimEx Base	"V1" active base
Maximum anode current	$\sim 6\mu$A, gain variation $\pm 5\%$	$\sim 16\mu$A, gain variation $\pm 1\%$
Maximum output pulse	unknown	-4 V, (-80 mA/50 Ohm)
Divider current	170 μA at 1.5 kV	450 μA at 1.1 kV
Maximum linear count rate	30 kHz $\pm 5\%$	1.2 MHz $\pm 1\%$

the "V0" and "V1" versions: a factor of ~ 25 as compared to the PrimEx base. However, as compared to both original PrimEx base and earlier passive-divider "V0" base, the "V1" active-base design indicates a noticeable improvement of the gain stability of the complete PMT plus base system versus count rate.

As a final test, we also performed radiation tests of the active PMT base in Hall C during the Qweak operations in 2012. We have found no degradation of the base for a radiation dose of 100 kRad. Hence, we plan to build, test and use such active bases for all $PbWO_4$ crystals of the planned Neutral-Particle Spectrometer.

E. Radiation Effects

Nearly all the known crystal scintillators are sensitive to electromagnetic and hadronic radiation. Interaction of ionizing radiation with scintillation crystals creates radiation damage. The creation of radiation damage involves impurities and defects in the crystal. Accumulated radiation at high doses may significantly change their characteristics. The most common damage is radiation-induced light absorption or change of crystal transmittance caused by the formation of color centers. Radiation may also cause reduction in the scintillation light yield (damage of the scintillation mechanism), and, because the radiation dose may not be uniform, a change in the light response uniformity.

Studies show that the degradation in optical transmission is the most important effect of radiation damage. In most crystals, the observed loss in scintillation light output can be explained by a decrease in transmission. Therefore, the radiation hardness studies always first refer to measurements of the optical transmission of a scintillator irradiated by various types and doses of radiation.

Radiation damage is determined by both the instantaneous dose rate and the integrated dose. Within an electron scattering environment, the generated radiation doses, and thus those absorbed by any calorimeter crystals, at angles less than 10° are dominated by Moeller electrons and related Bremsstrahlung.

$PbWO_4$ is known as a fast, dense and highly radiation resistant scintillator. Hence, it was for instance selected for construction of electromagnetic calorimeters for the CMS, ATLAS, and ALICE detectors operating at the LHC at CERN. For $PbWO_4$ crystals, radiation effects have been tested in HEPI (Protvino, Russia), at Brookhaven National Laboratory, and at CERN. A radiation hardness study of $PbWO_4$ crystal blocks intended for the BTeV experiment [16] showed that the radiation damage indeed depends on the dose rate (Rad/unit of time) for crystals irradiated by pure, intense high energy electron and hadron beams, as well as by a mixture of hadrons, neutrons and gammas.

The dedicated radiation dose studies showed that the $PbWO_4$ crystals degraded only by 2-3% for low dose rates, 15-20 krad/hr or less, and integrated doses below 10 krad [11]. Radiation damage dramatically increases at high doses. For example, while at a dose rate of 100 krad/hr the radiation damage amounts to $\sim 5\%$, the crystal degradation can reach 10-25% at instantaneous dose rates of ~ 500 krad/hr and integrated doses of 1-2 Mrad [11, 12]. Without exceptions, the loss of resolution is attributed to a degradation of the transmission properties of the crystals themselves, and not to the degradation of the photocathode of the PMTs.

Clear observations of the degradation of the light output as a function of dose have been reported in several papers. Nearly all the studies agree that at any given dose rate, after some irradiation time the degradation effects saturate. The level of the degradation scales with the dose rates. As an example, in Fig. 19 we show the results of a group at CMS [26]. For Nb/Y-doped $PbWO_4$ crystals, they measured the light output as a function

of irradiation time for varying dose rates: 15, 100, 500 and 1000 rad/h. The light output was normalized to that before irradiation.

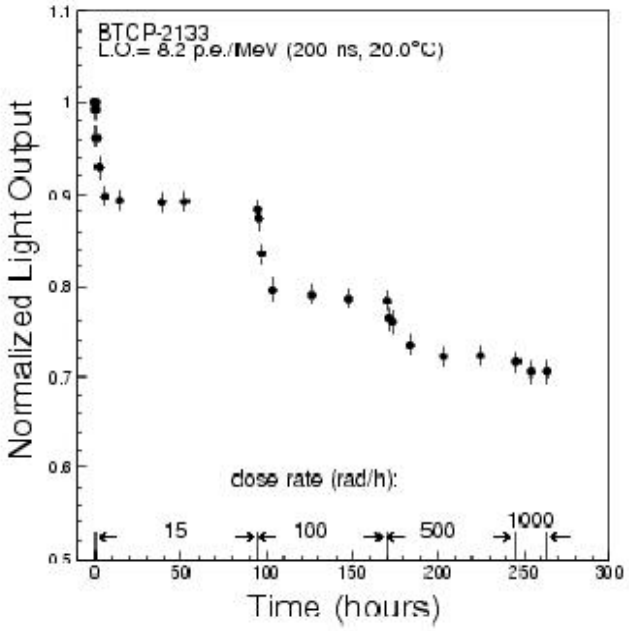

FIG. 19: *Light output as a function of irradition time for dose rates of 15, 100, 500 and 1000 rad/h, for a sample of Nb/Y-doped $PbWO_4$ crystals from BTCP. (Adopted from Qu Xiangdong Ph.D. Thesis [26]).*

A clean saturation behavior of the degradation effect can be seen for each of these dose rates. For this particular $PbWO_4$ crystal and a dose rate of 15 rad/h, a fast degradation of the normalized light output of ∼10% can be seen. The degradation then remains unchanged for the next 100 hours of radiation. After the radiation dose is changed from 15 to 100 rad/h, the light yield drops another 10% making the total degradation effect ∼20%, and then remains at this level for the next 70 hours of exposure. This pattern repeats with the next changes in radiation dose, from 100 rad/h to 500 rad/h, and finally to 1000 rad/h, although drops in light yield become less. Although the scale of degradation varies from crystal to crystal and depends on radiation dose, the behavior shown is common. Thus, careful studies and tests of samples of $PbWO_4$ with varying impurities, types and amount of doping materials are needed to select the proper crystals given particular radiation conditions and exposition times.

To improve the radiation resistance of the crystals usually they are doped with a small amount (40-100 ppm) of Nb, La, Lu, Y, Gd, Al or Ce at different stages of the growth process. Pentavalent Niobium (Nb) doping in $PbWO_4$ was first reported by Lecoq *et al.* to be effective in improving the transmittance at a level of 100 ppm [5]. Trivalent Lanthanum (La) doping was reported by Kobayashi *et al.* to be effective in improving transmittance and radiation hardness [27]. These pioneering studies were followed by studies with various other ions and their combinations, to further improve optical quality and radiation resistance of the crystals [5, 28, 29]. Perhaps not surprising given this situation, measurements indicate that $PbWO_4$ crystals produced by different manufactures may have significantly different properties, depending on the concentration and type of doped impurity.

The background radiation was further found to have strong negative impact on the optical properties of the crystals. Effects of this radiation damage again depend on the dose rate, the integrated dose, and the type of particles casuing the dose. At doses of more than 100 krad ($>$ 1 kGy), clear differences in the light transmission characteristics of the crystals exposed to protons have been observed as compared to photons. In proton-irradiated crystals, the band-edge (in light transmission versus wave length) shifts towards longer wavelength, while this band-edge remains stable in photon-irradiated crystals. Photon-induced damage saturates after a few

hours of exposure at a dose rate of ∼100 krad/h (1 kGy/h), while proton-induced damage increases linearly [24]. In addition, hadron irradiation may cause the crystals to become radioactive (due to the creation of nuclear fragments).

The transmission for samples of $PbWO_4$ crystals both before and after an integrated dose of 2 Mrad was measured in [17]. The results are shown in Fig. 20, and indicate only a ∼15-20% degradation in the wave length range of λ ∼350-400 nm, even at such a high integrated dose. Zhu *et al.* [18] studied the effect of integrated radiation dose for the $PbWO_4$ crystal for the LHC detectors, where dose rates of $\sim 15-500$ rad/h were expected. They reported that for $PbWO_4$ crystals the light output and slope did not show change up to an integrated dose of ∼2.2 Mrad (see Fig. 21). Similar results were observed in studies of the CMS Electromagnetic Calorimeter Group [19]. Comparison of luminiscence spectra measured both before and after an 100 krad photon irradiation (with a dose rate of ∼3.5 krad/hr) did not show any changes or damage to the scintillation mechanism.

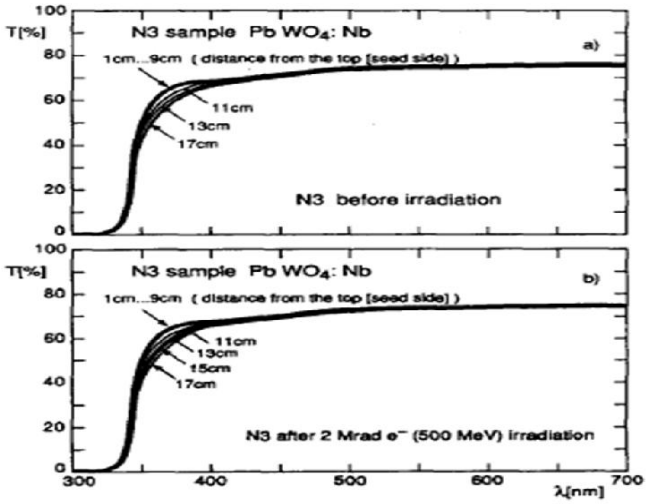

FIG. 20: *Transmission for samples of $PbWO_4$ crystals both before and after integrated doses of 2 Mrad. (Adopted from A. Fyodorov et al. [17]).*

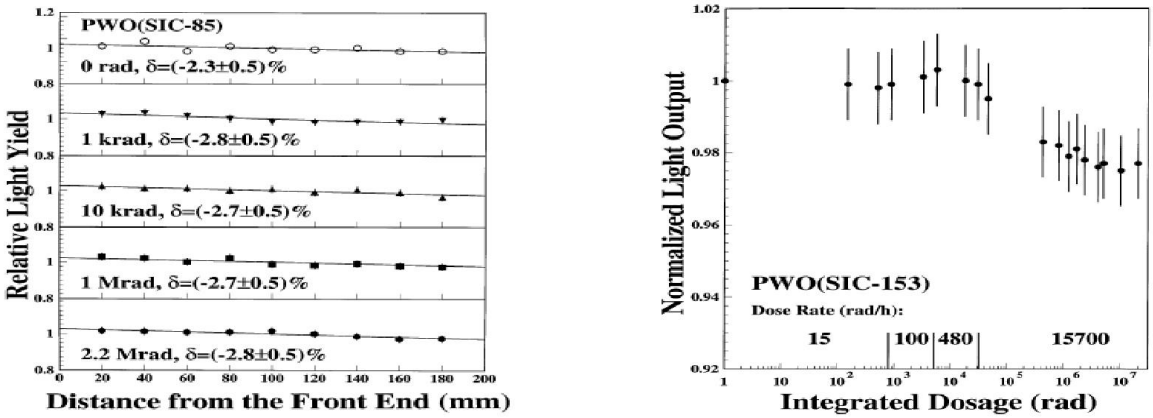

(a) (b)

FIG. 21: *(a) The light response as a function of distance from the front end of the crystal at different integrated radiation doses. (b) The normalized light output of a $PbWO_4$ crystal as a function of integrated dose. (Adopted from [18]).*

These results confirm that the scintillation mechanism is not damaged, and possibly only the front (few cm) of the crystals was subject to the radiation dose. A threshold behavior of radiation damage was observed, *i.e.* only particles above a certain energy appear to cause damage. For instance, the radiation damage due to

fast hadrons seems parameterized in terms of their inelastic interaction rate, rather than the hadron flux. Since the crystal contains heavy elements, fast hadrons (above ∼20 MeV) will produce heavy fragments. The energy loss of these slow fragments will amount to ∼50000 times those for minimum-ionizing particles.

Low energy neutrons (<20 MeV) do not cause significant damage to the crystals. The effect of an intense neutron flux on $PbWO_4$ crystals was studied in nuclear reactors (see Ref. [20], [21] and [22]). No significant effect was found up to flux densities of 10^{14} cm$^{-}2$. Even at very high neutron fluxes, of the order of $10^{19} - 10^{20}$ neutrons/cm^2, and extremely high doses of 330 MGy (33000 Mrad), the $PbWO_4$ crystals remained scintillating [23].

Some irradiated crystals can naturally recover transmission with time, at room temperature. However, such recovery is very slow, especially in the short wavelength region. The damage in $PbWO_4$ is thermally annealable, as well as optically bleachable [25]. For most of crystals almost complete recovery in transmission can be obtained after thermal annealing at temperature 200-500^o C.

A more suitable way of recovery is optical bleaching by ultraviolet (UV) or visible light. Such recovery is very effective for all crystals and can be implemented in situ. Almost full recovery in the transmission can be reached after exposure to light, ranging from tens of minutes to several hours, all depending on the intensity of the light source at a specifically selected wavelength. Even after multiple recovery the light yield and timing properties of the crystals remains nearly unchanged, and similar as for a non-irradiated crystal.

F. Radiation Doses

Radiation dose rates from Pavel Degtiarenko's realistic background simulation have been used to estimate the exact radiation condition as seen by the $PbWO_4$ detector as part of the NPS facility. We take into account the major sources of radiation: photons, electrons and positrons (since neutron radiation is moot, see the previous Section).

On the right hand side of the earlier presented particle background rates, a scale is added to indicate the radiation doses for a detector at a distance of 1 meter (under the assumed 1 μA current and 6 GeV energy beam, and for a 10 cm LH2 target). For a detector at a distance of 4 m from the target, these radiation doses scale down by a factor of 16. However, these paticle background rates and thus the dose rates are without taking into account the effect of a sweeping magnet. To estimate doses with such a magnet ON as compared to magnet OFF, the dose rates for electrons and positrons were scaled down proportional to the changes in their flux, taken from the simulated distributions with a threshold of 1 MeV.

The realistic background simulations were then cross-checked for an 11 GeV beam energy, with backgrounds found to be very similar (slightly reduced, by ∼10%) as compared to a 6.6 GeV beam energy. This is because the background is predominantly induced by the beam-target interactions, with the envisioned beam pipe only contributing 10-20%. Thus, we have further used the detailed background simulations at 6.6 GeV beam energy, which are well valid for a range of beam energies of ∼6 to 11 GeV.

In Fig. 22 we show the dose rates from photons, electrons, positrons and the total dose versus NPS angle, without sweeper magnet in the top panel, and with 0.3 Tm magnet in the bottom panel (rescaled based on the realistic simulated background fluxes). In Fig. 23 we then show the total dose rates as a function of NPS angle, with magnet on and off, compared to a 50 krad dose limit before UV curing is required, which we feel is a conservative number based on all studies presented (see Fig. 21).

The 50 krad dose limit is conservative as (i) even at much higher integrated doses only small (few %) effects are seen in Fig. 21; (ii) we do not take into account any additional shielding materials; and (iii) actual dose rates out-of-plane are much reduced. In addition, we integrated over all the low-energy particles included in the realistic background simulations, when in reality one would not anticipate much damage from electrons with energies below 1-2 MeV.

At the smallest NPS angle of 5.5^o the dose rate is ∼400-500 rad/hr for the sweeping magnet field OFF and ∼40-50 rad/hr for the field ON configuration, assuming a 1 μA beam current and a 10 cm LH2 target. Thus, one can take these numbers and the conservative 50 krad dose limit and scale to what can be considered acceptable

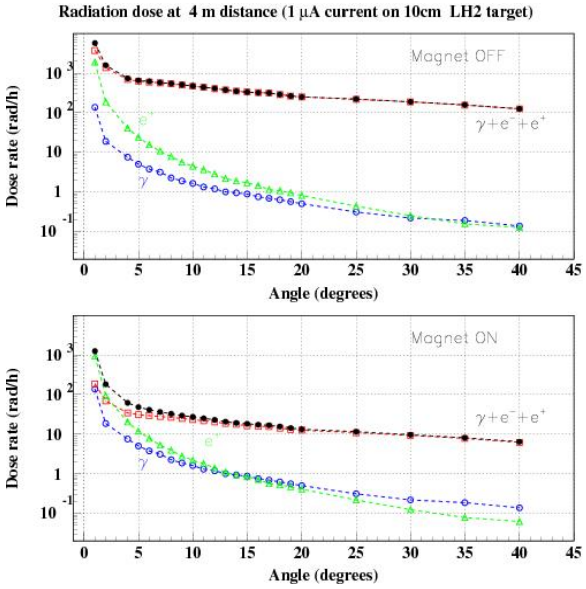

FIG. 22: *NPS detector Radiation dose rates from photons, electrons and positrons, and combined dose rates as a function of angle with sweep magnet OFF (top)and ON (bottom). The detector is at the distance of 4 m from the 10 cm LH2 target. The beam energy and current are 6.6 GeV and 1.0 μA.*

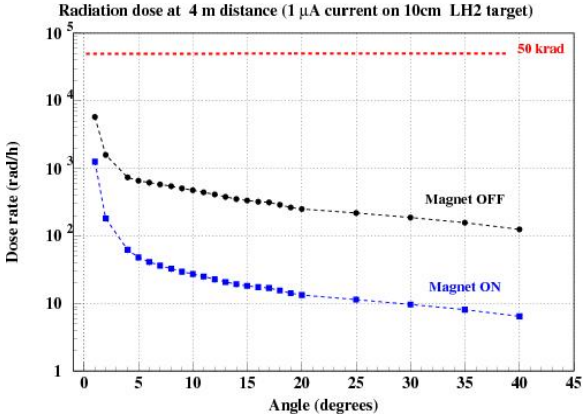

FIG. 23: *NPS detector Combined Radiation dose rates from photons, electrons and positrons as a function of angle, with sweep magnet OFF and ON. The detector is at the distance of 4 m from the 10 cm LH2 target. The beam energy and current are 6.6 GeV and 1.0 μA.*

running (luminosity) conditions. Or, if light output variations of up to a few % are acceptable for the physics of interest, one can relax the conservative 50 krad dose limit somewhat, possibly to a few 100 krad dose limits *.

* The energy spectrum and flux of the background particles were used to calculate the dose rates. For simplicity, we used the energy deposition of the particles in a small front surface layer of the $PbWO_4$ detector to normalize to 1 kg of matter. This is because the realistic background calculations performed by Pavel Degtiarenko of the JLab Radiation Control group uses as units Rem/hours (or Rad/hours) for dose rates, which corresponds to a 1 J energy deposition in 1 kg of matter. Hence, those dose rates correspond as calculated to those doses accumulated in frontal area of the $PbWO_4$ crystals. The simulations as performed do not provide information about the fall-off of radiation dose distribution along the thickness of the $PbWO_4$ crystals yet, as initial layers of the crystal will act as a shield for the deeper layers. This is another reason why our estimated dose rates are conservative as presented.

[1] Physics Opportunities with the 12 GeV Upgrade at Jefferson Lab, J. Dudek et al., Eur. Phys. J. A48 (2012) 187.
[2] M.E. Christy et al., Phys. Rev. C70 (2004) 015206.
[3] A Precision Measurement of the Neutral Pion Lifetime via the Rrimakov Experiment, JLab Proposal E02-103, A. Gasparian, S. Danagoulian spokespersons.
[4] M. Kubantsev et al., Performance of the Primex Electromagnetic Calorimeter, arXiv:physics/0609201, 22 Sep. 2006; A. Gasparyan, Performance of PWO crystal Detector for a High Resolution Hybrit Electromagnetic Calorimeter at Jefferson Lab., Proceed. X Int. Conf. Calorimetry in Particle Physics, Perugia, Italy, 29 March-2 April 2004, pp. 109-115.
[5] P. Lecoq et al., Nucl. Instr. and Meth. A 365, 291 (1994); A402, 75 (1998); A403, 302 (1998). .
[6] Shi Chao-Shu, Chin. Phys. Lett. **15**, 55 (1998).
[7] G. Franzoni et.al, Nucl. Instrum. Meth. A628, 90 (2011).
[8] R. Niyazov et al., Inner Calorimeter in CLAS/DVCS Experiment, Proc. of the Int. Workshop Exclusive Reactions at High Momentum Transfer, JLab, Newport News, VA, 21-24 May 2007, pp.421-424; V. D. Burkert et all., CEBAF experiment E01-113
[9] Measurement of the Ratio $R = \sigma_L/\sigma_T$ in Exclusive and Semi-Inclusive π° Production, Proposal to Jefferson Lab PAC38/PAC39, T. Horn, R. Ent, H. Mkrtchyan spokespersons.
[10] P. Bosted, R. Ent, and H. Mkrtchyan, Measurement of the Ratio R=σ_L/σ_T in Semi-Inclusive Deep-Inelastic Scattering, proposal to Jefferson Lab PAC30.
[11] L. Nagornaya et al., IEEE Transactions on Nuclear Science, Vol. 44, No. 3, p.866, June 1997.
[12] R. Y. Zhu et al., IEEE Transactions on Nuclear Science, Vol. 45, No. 3, p.686, June 1998.
[13] Pavel Degtiarenko, private communication.
[14] Bitao Hu, The analysis of primex test run on September 15. PRIMEX analysis documentation.
[15] V. Popov, H. Mkrtchyan, New potomultiplier active base for Hall C Jefferson Lab Lead Tangstate Calorimeter, NSSS2012-1098.
[16] V. A. Batarin et.al, (BTeV electromagnetic calorimeter group), Nucl. Instrum. Meth. A512, 488 (2003), hep-ex/0210011.
[17] A. Fyodorov et al., Rad. Meas. 26, 107 (1996)..
[18] R. Y. Zhu et al. Nucl.Instrum.Meth, A 413, 297 (1998)
[19] P. Adzic et al., The CMS Electromagnetic Calorimeter Group report, http://iopscience.iop.org/1748-0221/5/03/P0310, 2010.
[20] R. Chipaux et al., Proc. Mat. Res. Soc. Symp. 348 (1994) 481
[21] R. Chipaux and O. Toson, Proc. Int. Conf. Intorg. Scint. Appl., 1,(1995) 274
[22] M. Kh. Ashurov et al., Atom. Energy 91 (2001) 560
[23] R. Chipaux et al., Proc. 8th Int. Conf. Inorg. Scint.pg.369-371, Alushta, 2005
[24] H.Huhtinen et al., ETHZ-IPP-PR-2004-03, Swiss Institute for Particle Physics
[25] R. Y. Zhu et al., Nucl. Instr. and Meth. A376, 319 (1996); C. Woody et al., Proc. of SCINT95 Int'l Conf. Delft, August 1995 and IEEE-NUCL-S V43 (1996) 1585.
[26] Qu Xiangdong, A Study of Lead Tungstate Crystals and Improvement of Radiation Hardness. Ph.D. Thesis, Shanghai Institute of Ceramics. The Chinese Academy of Sciences, Shanghai, China, January 16, 2001.
[27] M. Kobayashi et al., Nucl. Instr. and Meth. A 406, 442 (1998); A 404, 149 (1998); A 399, 261 (1997); A 373, 333 (1996)
[28] S. Baccaro et al., Proc. SCINT97, Shanghai (1997) 203.
[29] M. Nicl et al., Phys. Stat. Sol. A164 (1997) R9; J. Appl. Phys. Lett. 82(11), 5758 (1997); J. Appl. Phys. Lett. 71,(26), 3755 (1997).